J. Fluid Mech. (2008), *vol.* 603, *pp.* 151–178.
doi:10.1017/S0022112008001043 Printed in the United Kingdom

Self-similar solutions of unsteady ablation flows in inertial confinement fusion

C. BOUDESOCQUE-DUBOIS, S. GAUTHIER
AND J.-M. CLARISSE
CEA/Bruyères-le-Châtel, 91297 Arpajon Cedex, France

(Received 22 March 2007 and in revised form 12 February 2008)

We exhibit and detail the properties of self-similar solutions for inviscid compressible ablative flows in slab symmetry with nonlinear heat conduction which are relevant to inertial confinement fusion (ICF). These solutions have been found after several contributions over the last four decades. We first derive the set of ODEs – a nonlinear eigenvalue problem – which governs the self-similar solutions by using the invariance of the Euler equations with nonlinear heat conduction under the two-parameter Lie group symmetry. A sub-family which leaves the density invariant is detailed since these solutions may be used to model the 'early-time' period of an ICF implosion where a shock wave travels from the front to the rear surface of a target. A chart allowing us to determine the starting point of a numerical solution, knowing the physical boundary conditions, has been built. A physical analysis of these unsteady ablation flows is then provided, the associated dimensionless numbers (Mach, Froude and Péclet numbers) being calculated. Finally, we show that self-similar ablation fronts generated within the framework of the above hypotheses (electron heat conduction, growing heat flux at the boundary, etc.) and for large heat fluxes and not too large pressures at the boundary do not satisfy the low-Mach-number criteria. Indeed both the compressibility and the stratification of the hot-flow region are too large. This is, in particular, the case for self-similar solutions obtained for energies in the range of the future Laser MegaJoule laser facility. Two particular solutions of this latter sub-family have been recently used for studying stability properties of ablation fronts.

1. Introduction

Ablation fronts appear when a directed high-energy density is released in a dense material. As a result, a supersonic thermal wave propagates and, as the sound speed ahead approaches the celerity of the thermal front, becomes subsonic while a shock wave is generated. At the same time, an expansion wave takes place and propagates in the opposite direction. This is the deflagrative heat wave (Pakula & Sigel 1985) in which the material is strongly accelerated while the density increases in the front and strongly decreases in the rear. This process is used to strongly compress a pellet in inertial confinement fusion (ICF) (Atzeni & Meyer-ter-Vehn 2004) in which the directed high-energy density is provided by a set of laser beams. However, the energy is not deposited uniformly on the pellet, perturbations are generated and may grow with time. These hydrodynamic instabilities at the ablation front called 'ablative Rayleigh–Taylor' (RT) instabilities, when the flow is accelerated, or 'ablative Richtmyer–Meshkov' instabilities (Goncharov 1999), when acceleration is negligible, are a key issue in ICF since they can inhibit burn. The first estimate

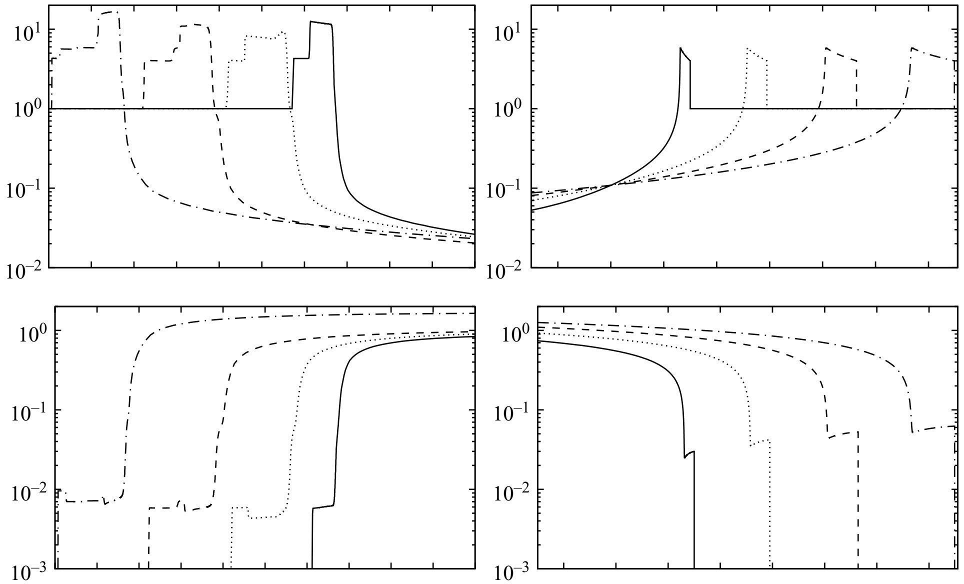

FIGURE 1. Density (top) and temperature (bottom) profiles obtained from a numerical simulation of a 0.1 mm thickness CH_2 planar foil illuminated with laser light (left). The same profiles obtained from the self-similar solution detailed in this paper have also been represented on the right-hand side. The thermal front propagates from right to left for the numerical simulation and from left to right for the self-similar solution. Profiles are plotted with respect to the x-coordinate. Self-similar profiles show a striking resemblance to the numerical simulation profiles.

of an ablation front instability growth has been given by Nuckolls *et al.* (1972) and the first model developed by Bodner (1974). Since then, a large number of studies have been devoted to this phenomenon. Stability analysis requires us to define or build a mean flow from which a perturbation analysis can be carried out. In that respect, Manheimer & Colombant (1982) built steady-state planar ablative flows and related flow quantities to laser characteristics. Kull & Anisimov (1986) developed a discontinuity model for describing incompressible RT instabilities with ablative mass and heat flow. The stability analysis of this mean flow was carried out analytically, whereas the analysis of the continuous version of this model, i.e. with a nonlinear diffusion term, was solved numerically (Kull 1989). This quasi-incompressible steady state provided the framework for many further stability analyses. Le Métayer & Saurel (2006) determined analytical solutions of steady ablation flows both within the low Mach number quasi-isobaric assumption and the fully compressible case.

However, mean flows encountered in ICF are usually neither steady nor quasi-incompressible. Instead they are closely related to self-similar behaviours as Velikovich *et al.* (1998) pointed out. This is illustrated in figure 1 (left) where we have represented density (top) and temperature (bottom) profiles obtained from a numerical simulation, at short times, of a 0.1 mm thickness CH_2 planar foil illuminated with laser light. Density and temperature profiles obtained from the self-similar solution detailed in this paper have also been represented in figure 1 (right). From these figures, it is clear that the flow is not steady and becomes closer to a self-similar profile as time goes on. Note that the density maximum keeps roughly the same level. In this simulation, the heat flux imposed at the boundary is piecewise linear and the slopes increase with time.

Marshak (1958) first found exact self-similar solutions from Euler's equations including radiation for constant density or constant temperature. Anisimov (1970) studied the case of a thermal wave in a two-temperature plasma, and gave the temperature, density and velocity variations as power laws in the time variable. Barrero & Sanmartín (1977) and Sanmartín & Barrero (1978*a*,*b*) expressed explicitly these variations for a two-temperature model with laser energy deposition evolving linearly in time. J.-M. Reisse, in Brun *et al.* (1977), exhibited, from numerical simulations, self-similar solutions of Euler's equations with nonlinear heat diffusion, provided that boundary conditions for the pressure and the heat flux are specific power laws in time. A first attempt to find these solutions had been made by Bajac (1973), but it seems that Y. Saillard, in an unpublished work of 1983, was the first to work out and write down the set of ODEs governing this family of self-similar solutions and to solve numerically this system with a finite-difference method (see also Boudesocque-Dubois *et al.* 2001, 2006; Abéguilé *et al.* 2006). Similar solutions of this type have also been determined by other workers. Reinicke & Meyer-ter-Vehn (1991) found self-similar solutions for strong point explosions provided that the ambient gas density decays with a given power of the radius. Sanz, Piriz & Tomasel (1992) studied a nonlinear heat-conduction one-temperature model with a different set of boundary conditions, and provided approximate piecewise solutions from asymptotic expansions. Murakami, Sakaiya & Sanz (2007) studied another family of self-similar solutions to model the acceleration phase.

The objective of this paper is twofold. We first describe in detail the present family of self-similar solutions of the Euler equations with nonlinear heat conduction, for the case of electron heat conduction. This discussion is quite general and is not related to a specific flow. Indeed it goes beyond the sole scope of ICF-type flows. We focus on the subsonic sub-family which leaves the density invariant. This solution is a nonlinear wave made up of two parts, an isothermal shock wave (Landau & Lifchitz 1987) bringing the material to high temperature and pressure, followed by an ablation front and an expansion wave. Since the flow through the front is subsonic, this solution is close to a deflagration wave (Thompson 1988). A chart allowing us to determine the starting point of a numerical solution, knowing the physical boundary conditions, has been built with more than 300 self-similar solutions for electron heat conduction and an adiabatic exponent $\gamma = 5/3$. An approximate scaling law, which connects the absolute Mach number at the ablation front to the heat flux at the origin is given. In a second step, the deflagration density-invariant sub-family of self-similar solutions is applied to ICF. Such a deflagration wave is encountered in the implosion of a pellet in ICF during the 'early-time' period where a shock wave travels from the front to the rear surface of the target. The importance of this 'early-time' period has been emphasized by several authors (Aglitskiy *et al.* 2002; Velikovich *et al.* 2000), since perturbations growing during this period will set the initial conditions or the seeds for the subsequent acceleration phase. The deflagration density-invariant sub-family may be used to model such a flow. Self-similar compatible boundary conditions are then imposed at the origin of the Lagrangian coordinate, assimilated here to the critical surface of laser energy absorption. This hypothesis is clearly an approximation in the case of a direct illumination by laser light, but exact for a radiative heat conduction in the case of irradiation by X-ray light, a configuration which will be studied elsewhere. An example of the determination of self-similar solution constants is described by using a multiphysics numerical simulation of a flow relevant to the Laser MegaJoule

(LMJ) laser facility. Finally we show that these LMJ self-similar solutions do not satisfy the constraints of the low-Mach-number approximation (Paolucci 1982; Majda & Sethian 1985; Fröhlich & Gauthier 1993) often used in stability analyses of ablation fronts in ICF, although quasi-incompressible self-similar solutions may be obtained for lower heat fluxes and/or larger pressures at the boundary. These families of self-similar solutions – whether they be density or temperature invariant – may be of interest in other configurations relevant to ICF (Pakula & Sigel 1985). Since these solutions are to be used for carrying out stability analyses (Abéguilé *et al.* 2006), a high accuracy is required for mean flow quantities and their derivatives. A numerical algorithm, based on an auto-adaptive multidomain Chebyshev method, has therefore been devised (Gauthier *et al.* 2005) and is summarized in Appendix B.

2. Governing equations and self-similar formulation

2.1. *One-dimensional Euler equations with nonlinear heat conduction*

Consider the motion of an inviscid heat-conducting fluid, obeying the polytropic equation of state:

$$p = \rho R T, \qquad \mathscr{E} = \frac{R}{\gamma - 1}\mathrm{T}, \tag{2.1}$$

where ρ is the fluid density, p the fluid pressure, $\mathscr{E}$ the specific internal energy, T the fluid temperature, R the gas constant and γ the fluid adiabatic exponent. For one-dimensional motions in the x-direction, the Euler equations of motion can be written, in Lagrangian form, as

$$\left.\begin{aligned} &\frac{\partial}{\partial t}\left(\frac{1}{\rho}\right) - \frac{\partial}{\partial m} v_x = 0,\\ &\frac{\partial}{\partial t} v_x + \frac{\partial}{\partial m} p = 0,\\ &\frac{\partial}{\partial t}\left(\frac{1}{2} {v_x}^2 + \mathscr{E}\right) + \frac{\partial}{\partial m}\left(p v_x + \varphi_x\right) = 0, \end{aligned}\right\} \tag{2.2}$$

where the Lagrangian coordinate m is such that $\mathrm{d}m = \rho\,\mathrm{d}x$, and v_x is the fluid velocity. The heat flux φ_x is

$$\varphi_x = -\kappa(\rho, T)\,\frac{\partial T}{\partial x} = -\kappa(\rho, T)\,\rho\,\frac{\partial T}{\partial m}, \tag{2.3}$$

where the thermal conductivity coefficient κ depends on the density ρ and temperature T through

$$\kappa(\rho, T) = \kappa_0 \left(\frac{\rho}{\rho_c}\right)^{-\mu} \left(\frac{T}{T_c}\right)^{\nu}, \tag{2.4}$$

and μ, ν are fluid constants to be chosen such that $\mu \geqslant 0$ and $\nu \neq 1$, ρ_c and T_c are characteristic density and temperature of the flow, κ_0 is the thermal conductivity coefficient for $\rho = \rho_c$ and $T = T_c$, which gives the thermal diffusivity coefficient $\chi = (\gamma - 1)\kappa_0/\gamma \rho_c R$. System (2.2) is supplemented by initial and boundary conditions which will be defined later.

2.2. *Self-similar formulation*

Following Zel'dovich & Raizer (1967), we observe that the only dimensionless combination that can be obtained from the Lagrangian coordinate m, the time t

and the parameters of the problem ρ_c, R, χ and the isothermal sound speed c_*, is

$$\xi = \frac{m\, t^{-\alpha}}{\rho_c\, \mathfrak{b}} \quad \text{with } \mathfrak{b} = \chi^{1-\alpha} c_*^{2\alpha-1}. \tag{2.5}$$

The characteristic temperature T_c is then defined as $T_c = c_*^2/R$. We are looking for the Lie group symmetry under which system (2.1)–(2.4) is invariant. This group of similitude depends on seven parameters and may be written as

$$\left.\begin{array}{llllll} m' = \lambda^{E_m} & m, & {v_x}' = \lambda^{E_{v_x}} & v_x, & t' = \lambda^{E_t} & t, \\ \rho' = \lambda^{E_\rho} & \rho, & p' = \lambda^{E_p} & p, & & \\ T' = \lambda^{E_T} & T, & {\varphi_x}' = \lambda^{E_{\varphi x}} & \varphi_x, & & \end{array}\right\} \tag{2.6}$$

where we have introduced one more parameter λ, which will be determined later. The fact that (2.1)–(2.4) should be unchanged by the transformation (2.6) introduces five constraints, which are written as

$$\left.\begin{array}{ll} E_m = -\mu\, E_\rho + (2\nu - 1)\, E_{v_x}, & \\ E_t = -(\mu + 1)\, E_\rho + 2(\nu - 1)\, E_{v_x}, & E_p = E_\rho + 2\, E_{v_x}, \\ E_T = 2\, E_{v_x}, & E_{\varphi_x} = E_\rho + 3\, E_{v_x}. \end{array}\right\} \tag{2.7}$$

Any dependent variable $\mathscr{H}(m, t)$ is transformed under the group as

$$\mathscr{H}'(m', t') = \lambda^{E_h}\, \mathscr{H}(\lambda^{E_m} m, \lambda^{E_t} t). \tag{2.8}$$

The free parameter λ is defined in such a way that $\mathscr{H}$ depends on only a single variable. This is achieved by using $t \propto \lambda^{-E_t}$. Then the self-similar variable is defined by (2.5) where $\alpha = E_m/E_t$. Introducing this self-similar variable ξ and time power law dependencies for the physical variables, we obtain the reduced function definitions

$$\left.\begin{array}{lll} \rho = \rho_c & t^{\alpha-\beta} & G(\xi), \\ v_x = \mathfrak{b} & t^{\beta-1} & V(\xi), \\ T = \dfrac{\mathfrak{b}^2}{R} & t^{2(\beta-1)} & \Theta(\xi), \\ \varphi_x = \rho_c \mathfrak{b}^3 & t^{\alpha-\beta+3(\beta-1)} & \Phi(\xi), \end{array}\right\} \tag{2.9}$$

with

$$\alpha = \frac{-E_\rho \mu + E_{v_x}(2\nu - 1)}{-E_\rho(\mu + 1) + 2E_{v_x}(\nu - 1)}, \quad \beta = \frac{-E_\rho(\mu + 1) + E_{v_x}(2\nu - 1)}{-E_\rho(\mu + 1) + 2E_{v_x}(\nu - 1)}. \tag{2.10}$$

The system obtained from (2.1)–(2.4) reduces then to the fourth-order ODE

$$\frac{\mathrm{d}}{\mathrm{d}\xi}\left(\frac{\alpha\,\xi}{G} + V_x\right) = \frac{\beta}{G}, \tag{2.11a}$$

$$\frac{\mathrm{d}}{\mathrm{d}\xi}(\alpha\,\xi\, V_x - G\,\Theta) = (\alpha + \beta - 1)\, V_x, \tag{2.11b}$$

$$\frac{\mathrm{d}}{\mathrm{d}\xi}\left(\alpha\,\xi\left[\frac{{V_x}^2}{2} + \frac{\Theta}{\gamma - 1}\right] - G\,\Theta\, V_x - \Phi_x\right) = [\alpha + 2(\beta - 1)]\left(\frac{{V_x}^2}{2} + \frac{\Theta}{\gamma - 1}\right), \tag{2.11c}$$

$$\frac{\mathrm{d}\Theta}{\mathrm{d}\xi} = -\frac{\Phi_x}{G^{1-\mu}\,\Theta^{\nu}}. \tag{2.11d}$$

The similarities leaving invariant the equations of the problem form a two-parameter group $\mathfrak{G}_{(E_\rho, E_{v_x})}$. The subgroup $\mathfrak{G}_{(0, E_{v_x})}$ leaves invariant the density, whereas the subgroup $\mathfrak{G}_{(E_\rho,0)}$ leaves invariant the velocity and the temperature. The one-parameter group of similitude $\mathfrak{G}_{(E_\rho,0)}$ admits several invariants. Let $f(m,t)$ be an absolute invariant (Moran & Gaggioli 1968) which satisfies $f(m',t') = f(m,t)$. Expanding $f(m',t')$ in a Taylor series, it is straightforward to show that the invariant is the solution of the following equation

$$\left(\left.\frac{\partial m'}{\partial \lambda}\right|_{\lambda=1} \frac{\partial}{\partial m} + \left.\frac{\partial t'}{\partial \lambda}\right|_{\lambda=1} \frac{\partial}{\partial t} \right) f(m,t) = 0. \tag{2.12}$$

The solution to this equation is simply any function F of the variable $\xi = m/t^\alpha$. In particular, the reduced functions (2.9) are invariants.

Sets of initial and boundary conditions which are compatible with such a self-similar formulation (2.9) are such that (Brun *et al.* 1977):

$$\left.\begin{array}{rlcrl}
\rho(m,t=0) = C^I_\rho & m^{(\alpha-\beta)/\alpha} & \longrightarrow & G(\xi\to\infty) = C^I_\rho & \xi^{(\alpha-\beta)/\alpha}, \\
v_x(m,t=0) = C^I_v & m^{(\beta-1)/\alpha} & \longrightarrow & V_x(\xi\to\infty) = C^I_v & \xi^{(\beta-1)/\alpha}, \\
T(m,t=0) = C^I_T & m^{2(\beta-1)/\alpha} & \longrightarrow & \Theta(\xi\to\infty) = C^I_T & \xi^{2(\beta-1)/\alpha}, \\
\varphi_x(m,t=0) = C^I_\varphi & m^{(\alpha-\beta+3(\beta-1))/\alpha} & \longrightarrow & \Phi_x(\xi\to\infty) = C^I_\varphi & \xi^{(\alpha-\beta+3(\beta-1))/\alpha},
\end{array}\right\} \tag{2.13}$$

$$\left.\begin{array}{rlcr}
\rho(m=m_B,t) = C^B_\rho & t^{\alpha-\beta} & \longrightarrow & G(\xi = m_B t^{-\alpha}) = C^B_\rho, \\
v_x(m=m_B,t) = C^B_v & t^{\beta-1} & \longrightarrow & V_x(\xi = m_B t^{-\alpha}) = C^B_v, \\
T(m=m_B,t) = C^B_T & t^{2(\beta-1)} & \longrightarrow & \Theta(\xi = m_B t^{-\alpha}) = C^B_T, \\
\varphi_x(m=m_B,t) = C^B_\varphi & t^{3(\beta-1)} & \longrightarrow & \Phi_x(\xi = m_B t^{-\alpha}) = C^B_\varphi.
\end{array}\right\} \tag{2.14}$$

2.3. *Sub-family for invariant density*

At time $t = 0$, the fluid of uniform density ρ_c is assumed to occupy the half-space $m \geqslant 0$, while a heat flux starts being applied along the plane $m = 0$. Initial and boundary conditions are

$$\left.\begin{array}{rcl}
\rho & = & \rho_c \\
v_x & = & 0 \\
T & = & 0
\end{array}\right\} \quad \text{for } m \geqslant 0, \tag{2.15}$$

$$\left.\begin{array}{rcl}
p & = & p_* \left(\dfrac{t}{t_*}\right)^{2(\alpha-1)} \\
\varphi_x & = & \varphi_* \left(\dfrac{t}{t_*}\right)^{3(\alpha-1)}
\end{array}\right\} \quad \text{for } m = 0 \tag{2.16}$$

respectively, where p_*, φ_* and t_* are characteristic boundary pressure, heat flux and time. The choice of initial and boundary conditions given by (2.15)–(2.16) imposes on us the use of the subgroup $\mathfrak{G}_{(0,E_{v_x})}$. In this case, $\alpha = \beta = (2\nu - 1)/(2\nu - 2)$, and system (2.11) is given by

$$\frac{\mathrm{d}\boldsymbol{Y}}{\mathrm{d}\xi} = \mathscr{F}(\xi, \boldsymbol{Y}), \tag{2.17}$$

in terms of the unknown $\boldsymbol{Y}^{\mathrm{T}} = (G\ V\ \Theta\ \Phi)$. The function $\mathscr{F}$ is given by

$$\mathscr{F}(\xi, \boldsymbol{Y}) = \begin{pmatrix} G^2\, N/D \\ \alpha\xi\, N/D \\ F \\ (\alpha\,\xi\, F - 2(\alpha-1)\,\Theta)\,/(\gamma-1) - \alpha\,\xi\, G\,\Theta\, N/D \end{pmatrix}, \tag{2.18}$$

with:

$$\left.\begin{aligned} N &= (\alpha-1)\,V + G\,F, \\ D &= \alpha^2\,\xi^2 - G^2\,\Theta, \\ F &= -\Phi\, G^{\mu-1}\,\Theta^{-\nu}. \end{aligned}\right\} \tag{2.19}$$

Applying the Π-theorem (Barenblatt 1979), the seven parameters ρ_c, R, γ, χ, c_*, p_* and φ_* lead us to retain the three dimensionless numbers

$$\mathscr{B}_\varphi = \frac{\varphi_*}{\rho_c {c_*}^3}, \qquad \mathscr{B}_p = \frac{p_*}{\rho_c {c_*}^2}, \qquad \gamma. \tag{2.20}$$

The coefficient $\mathscr{B}_\varphi$ may be written as $\mathscr{B}_\varphi = \phi/(\rho\, v^3) v^3/c^3 = M^3/Cl$, where M is a Mach number and Cl the Clausius number, which is the ratio of the kinetic energy flux to the thermal conduction flux. For the solutions investigated in this work, the Clausius number is larger or smaller than one. Note that the parameter $\mathscr{B}_\varphi$ is similar to the parameter β^{-1} introduced by sanz *et al.* (1992). The corresponding dimensionless forms of (2.15) and (2.16) are

$$\left.\begin{aligned} G(\xi \to +\infty) &= 1, \\ V(\xi \to +\infty) &= 0, \\ \Theta(\xi \to +\infty) &= 0, \end{aligned}\right\} \tag{2.21}$$

and

$$\left.\begin{aligned} (G\Theta)(\xi = 0) &= \mathscr{B}_p, \\ \Phi(\xi = 0) \quad &= \mathscr{B}_\varphi, \end{aligned}\right\} \tag{2.22}$$

respectively. We consider solving the ODEs (2.17) in the domain $[0, +\infty)$ with boundary conditions (2.21)–(2.22). System (2.17) possesses different kinds of singularity. In the physical configuration considered (for adiabatic exponent $\gamma < 3$), only one case – the case $D = 0$ – can be encountered. Moreover, if we admit a zero temperature, the solution of (2.17) can be expressed explicitly: $V \propto \xi^{1-1/\alpha}$ and $G \propto \xi^{-1/\alpha} + \text{const}$. Note that D (2.19) changes sign over the domain $[0, +\infty)$ since $D(\xi \to \infty) > 0$ and $D(\xi = 0) < 0$. The problem raised by the presence of the singularity $D = 0$ may be circumvented by introducing a shock-wave discontinuity at an arbitrary point, say ξ_s.

Restriction to deflagration density-invariant sub-family

In the absence of any known analytical solution to system (2.17), we must have recourse to numerical methods for integrating (2.17) or the corresponding initial- and boundary-value problems (IBVPs). Numerical simulations of such IBVPs in the cases of radiation (Marshak 1958) or electron (Brun *et al.* 1977) heat conductions have shown that, for sufficiently low values of the boundary heat flux, the heated fluid region is bounded by an isothermal shock wave ‘together with an infinitesimal radiation wavelet' (Marshak 1958). Here we restrict ourselves to flows for which this wave combination is of negligible thickness, so that it may be replaced by a non-isothermal shock wave at the forefront of the heated fluid, thus leading to the jump relations (A1). This is the sole approximation conceded in this work. The mean-flow jump relations (A1) applied to the self-similar solution (2.9) lead to the expressions

$$G_D = \frac{(\gamma+1)W^2}{\gamma W^2 - \mathscr{R}}, \quad V_D = \frac{W^2 + \mathscr{R}}{(\gamma+1)W}, \quad P_D = \frac{W^2 + \mathscr{R}}{\gamma+1}, \tag{2.23}$$

for the downstream values of the self-similar functions G, V and P. In these formulae, the quantity $\mathscr{R}$ is given by

$$\mathscr{R} = \sqrt{W^4 - 2(\gamma-1)(\gamma+1)\, W\, \Phi_{xD}}\,, \tag{2.24}$$

where W is the self-similar shock-front velocity whose expression comes as

$$W = t^{1-\alpha} w_x = t^{1-\alpha} \left(\frac{\partial x}{\partial t}(m,t) \right)_{\xi} \Bigg|_{\xi_s} = \left(\frac{\alpha \xi}{G(\xi)} + V(\xi) \right) \Bigg|_{\xi_s}. \tag{2.25}$$

Integrating system (2.17) from $+\infty$ to ξ_s, with conditions at infinity provided by relations (2.21), leads to $D(\xi_s^+) = D(\xi \to \infty) > 0$. On the other hand, the Rankine–Hugoniot relations at ξ_s give that $D(\xi_s^-)$ is negative, for $1 \leqslant \gamma \leqslant 3$, so that the singularity $D = 0$ is effectively eliminated. An obvious consequence is that system (2.17) has now to be integrated over the domain $[0, \xi_s)$, with boundary conditions given by (2.22) and (2.23). This defines a nonlinear eigenvalue problem.

3. Obtaining the invariant-density sub-family

For a given value of the shock wave location ξ_s, integrating system (2.17) from ξ_s^- to the origin $\xi = 0$ furnishes pressure and heat flux boundary values, which, however, may not necessarily be the values $\mathscr{B}_p$ and $\mathscr{B}_\varphi$ defined by (2.20). In order to obtain these values, we have recourse to a shooting method. Note that knowing the values of $\mathscr{B}_p$ and $\mathscr{B}_\varphi$, we may think of integrating system (2.17) from 0 to ξ_s^-. With the help of $\mathscr{B}_p$ and $\mathscr{B}_\varphi$ and having in mind that all the components of $\boldsymbol{Y}(0)$ are not known, the shooting method may be started from the origin and stopped at a point where the Rankine–Hugoniot relations are best satisfied. The main drawback of this approach is that the ranges to be explored for the missing components of $\boldsymbol{Y}(0)$ – say $G(0)$ and $V(0)$ – are *a priori* infinite – $0 < G(0) < +\infty$ and $-\infty < V(0) < +\infty$.

Backward numerical integration of system (2.17) from ξ_s^- to 0, using either explicit or implicit methods, turns out to be unstable. The rather elaborate procedure that we now detail is a direct consequence of this. A possible approach for tackling this difficulty is suggested by previous studies (Barrero & Sanmartín 1977; Sanmartín & Barrero 1978*a*; Sanz et al.) on self-similar solutions to system (2.2). Therein, two regimes for the flow within the region between the origin ($\xi = 0$) and the shock wave front ($\xi = \xi_s$) were identified: (i) a regime where convection is dominant which corresponds to the flow region immediately downstream of the shock wave front; and (ii) a regime where heat conduction effects are important which is associated to the part of the flow extending from the origin, where the external heat flux is applied, towards increasing ξ-abscissae. Similar remarks led Y. Saillard, in an unpublished work of 1983, to introduce an arbitrary interior point ξ_f and to consider, on the domain (ξ_f, ξ_s), the system of ODEs (2.17) without heat conduction. The boundary conditions (2.21) and the Rankine–Hugoniot relations (A2) without conduction give a starting value for $(G\,V\,\Theta)$ at ξ_s^-. Integrating (2.17) without heat conduction from ξ_s^- to ξ_f^+ yields $\big(G(\xi_f^+)\,V(\xi_f^+)\,\Theta(\xi_f^+)\big)$, the corresponding values at ξ_f^- being deduced from continuity arguments, with $\Phi(\xi_f^-)$ given by $\Phi(\xi_f^-) = -\big(G^{1-\mu}\Theta^{\nu}(\mathrm{d}\Theta/\mathrm{d}\xi)\big)\,(\xi_f^-)$. System (2.17) can thus be integrated from ξ_f^- to 0.

This way of proceeding provides a first guess for a solution which depends on the two parameters ξ_f and ξ_s – these parameters having to be adjusted for recovering the values (2.20) of $\mathscr{B}_p$ and $\mathscr{B}_\varphi$. The approximations $\boldsymbol{Y}$ thus obtained suffer, however, a critical defect in that their derivatives $\mathrm{d}\boldsymbol{Y}/\mathrm{d}\xi$ are discontinuous at ξ_f. Indeed, these derivative values are involved in the computation of the solution perturbations (Abéguilé *et al.* 2006). Therefore, better approximations are required, leading us to devise the strategy developed in Appendix B, where an iterative method is used within the framework of a Chebyshev spectral method. A relaxation method is also used in order to minimize the error on the Rankine–Hugoniot relations at the shock wave. This algorithm has been implemented in the numerical code $\mathfrak{R}$amses. As a result, the system of ODEs for the reduced function (2.17) is accurately solved: the error is of the order of 10^{-9}, except at the shock-wave location where it reaches $10^{-4}-10^{-5}$, for a fifteen-digit floating-point number implementation. Such an accuracy is obtained using 8 to 12 subdomains (usually 10), depending on the parameter values, with 50 Chebyshev polynomials. Fewer than 100 iterations, usually 35, are required.

As already stated, we are interested in the solution of (2.17) where a shock wave, which bounds the domain, is followed by a thermal front. Across this shock, both the fluid density and velocity (owing to the zero viscosity of the physical model) are discontinuous. However, a nonlinear thermal conductivity dictates the shape of the thermal front (Zel'dovich & Raizer 1967, chap. 10, §3). Indeed the temperature profile is continuous and exhibits a preheating 'tongue' (cf §2.3) of estimated thickness

$$\Delta\xi_s = \frac{\gamma-1}{\nu}\,\frac{G\,\Theta^{\nu}}{V}, \tag{3.1}$$

assuming that the conductivity depends only on the temperature. This expression is obtained by retaining only the terms depending on the temperature in the energy equation and by looking for a standing-wave solution and then integrating twice. This thickness is, in any case, very small and the isothermal shock is described well by a perfect discontinuity. As we see in figure 2, the error between the solution at the shock front and the Rankine–Hugoniot relations may be related to the estimate of the thickness of the isothermal shock wave given by (3.1). In this figure, we have plotted the relative error on the Rankine–Hugoniot relations versus the estimated thickness of the isothermal shock wave given by (3.1). We have varied successively the exponents ν and γ, and obtained two monotonic curves, very close to each other. This shows that the error on the Rankine-Hugoniot at the shock wave is due to the isothermal shock wave thickness that is neglected.

The code $\mathfrak{R}$amses computes reduced functions by solving system (2.17). However, this system does not take into account the physical aspect of the mean flow. It is thus necessary to introduce some criteria of eligibility. Indeed, it has been noticed that there is an upper bound on the ξ_f values, ξ_f^{max}, beyond which we cannot obtain a physical solution with $G(\xi) > 0$. Furthermore, it has been noticed also that for flows obtained with small values of ξ_f, the heat flux at the origin could be negative. This allows us to obtain the lower value of ξ_f, ξ_f^{min}, such that the heat flux at the origin is positive: $\Phi(\xi=0) \geqslant 0$. With this criterion, we may thus eliminate the numerically accessible flows which are not representative of an ablative deflagration. Besides, it turns out that this condition is not sufficient. For very small values of ξ_s and ξ_f,

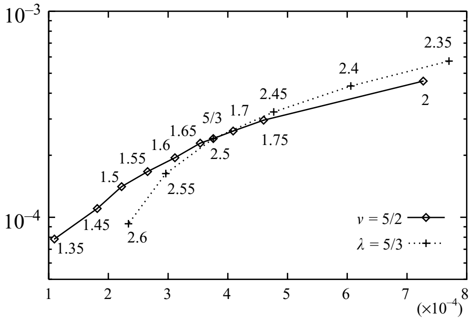

FIGURE 2. Relative error on the Rankine–Hugoniot relations *vs.* the thickness of the isothermal shock wave given by (3.1). The curve $\nu = 5/2$ has been obtained by varying the polytropic exponent γ, whereas the curve $\gamma = 5/3$ has been obtained by varying the exponent ν. The monotonicity of the two curves shows the relevance of the estimate (3.1) as the source of error on the Rankine–Hugoniot relations (2.23).

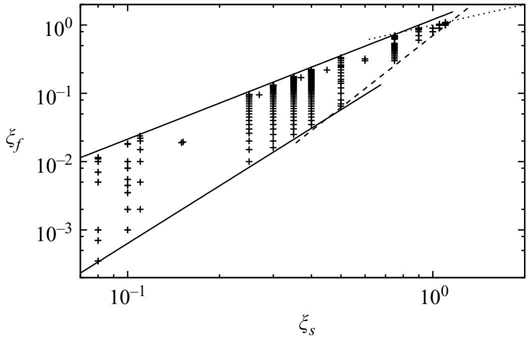

FIGURE 3. Eligible values of the origin ξ_f and the end ξ_s of the shocked-fluid zone, in the case of an electron heat conduction and $\gamma = 5/3$. The lower and upper bounds on ξ_f are estimated as functions of ξ_s (3.2).

we observe that in certain cases the ablation front has merged with the origin, i.e., the solution does not describe the expansion wave, hence does not agree with the assumptions of the model. Consequently, by denoting ξ_a the position of the ablation front (defined as the location of the density maximum), a new criterion appears to be: $\xi_a > 0$.

Figure 3 represents, in the case of electron heat conduction and $\gamma = 5/3$, about 300 pairs of data points (ξ_f, ξ_s). For a given value of ξ_s (on the abscissa), we represent all the eligible values of ξ_f. The upper and lower values of ξ_f are approximated by the following power laws

$$\xi_f^{min} = \begin{cases} a_1\,\xi_s^{b_1}, & \xi_s \leqslant \Xi_{min}, \\ a_2\,\xi_s^{b_2}, & \xi_s \geqslant \Xi_{min}, \end{cases} \qquad \xi_f^{max} = \begin{cases} A_1\,\xi_s^{B_1}, & \xi_s \leqslant \Xi_{max}, \\ A_2\,\xi_s^{B_2}, & \xi_s \geqslant \Xi_{max}. \end{cases} \tag{3.2}$$

All the coefficients $a_1, b_1, \ldots, \Xi_{max}$ depend on γ. For $\gamma = 5/3$, we have

$$\left.\begin{array}{lllll} a_1 = 0.4, & b_1 = 2.8, & a_2 = 0.7, & b_2 = 3.5 & (\Xi_{min} \approx 0.45), \\ A_1 = 1.2, & B_1 = 1.75, & A_2 = 1, & B_2 = 1 & (\Xi_{max} \approx 0.78). \end{array}\right\} \tag{3.3}$$

As an illustration of the whole method, two examples of self-similar solutions are given in figures 4 and 5. These two electron heat conduction solutions are obtained

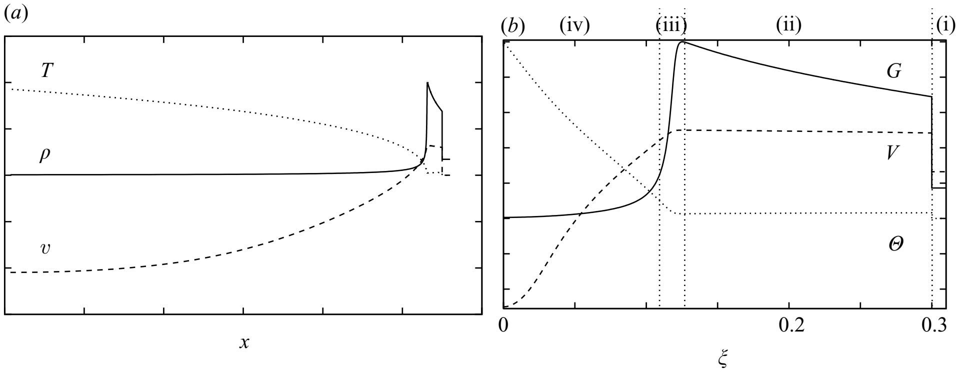

FIGURE 4. Structure of a self-similar flow in the case of a steep density gradient, $(\mathscr{B}_\varphi = 0.26, \mathscr{B}_p = 0.03, \gamma = 5/3)$. Density ρ, temperature T and velocity v are represented (*a*) *vs*. space at a given time, (*b*) by their reduced functions G, Θ and V. We can distinguish (i) the undisturbed fluid zone ($\xi > \xi_s$), (ii) the quasi-isentropic compression zone, (iii) the ablation layer and (iv) the conduction-dominated zone. This solution is within the range of energy of the LMJ facility. Note that the temperature of the fluid at rest is equal to zero.

for $\mu = 0$, $\nu = 5/2$ in (2.4), or equivalently $\alpha = 4/3$ in (2.5), and for a monatomic gas ($\gamma = 5/3$). The remaining dimensionless numbers $\mathscr{B}_p$ and $\mathscr{B}_\varphi$ are determined from a one-dimensional numerical simulation of the direct laser illumination of a planar target within the energy range of the LMJ facility. In such configurations, the self-similar solutions do not describe the flow expansion past the critical surface on which depend the values of the solution boundary parameters $\mathscr{B}_p$ and $\mathscr{B}_\varphi$.

In the present case, the numerical simulation has been carried out with the multiphysics hydrocode FCI1 (Fortin & Canaud 2000). The parameters $\mathscr{B}_p$ and $\mathscr{B}_\varphi$ are then determined in order to match, as closely as possible, the numerical simulation profiles. The empirical procedure determining the physical quantities involved in the expressions of $\mathscr{B}_p$ and $\mathscr{B}_\varphi$ (2.20) is the following. The knowledge of the laser intensity law gives the characteristic time t_* to be the time after which a second shock wave propagates from the front to the rear of the target. Then, we define a location x_*, where the deposited laser power is maximum at this particular time t_*. At this point (x_*, t_*), we retrieve the heat flux φ_*, fluid pressure p_*, thermal diffusivity coefficient χ and gas constant R. Using (2.20), we deduce the dimensionless number values $\mathscr{B}_p$ and $\mathscr{B}_\varphi$. We thus obtain the self-similar solution represented in figure 4. This solution corresponds to a large extent to the conduction region for a given location of the shock wave ξ_s. We can distinguish in figure 4(*b*) four zones: (i) the undisturbed fluid zone ($\xi > \xi_s$); (ii) the quasi-isentropic compression zone comprised between the ablation layer and the shock-wave front; (iii) the ablation layer with steep density gradients; and (iv) the conduction-dominated zone extending from the origin up to the ablation layer. However, the characteristic time t_* is approximately defined and a slight variation of its value leads to different values for ($\mathscr{B}_p$, $\mathscr{B}_\varphi$). An example of such a variation is provided in (Abéguilé *et al.* (2006), table I). Another example of self-similar solution is given in figure 5 in which the heat flux law is different from the previous example. This case (figure 5) corresponds to a small value of ξ_f for a given ξ_s: as a result, the density gradient is soft.

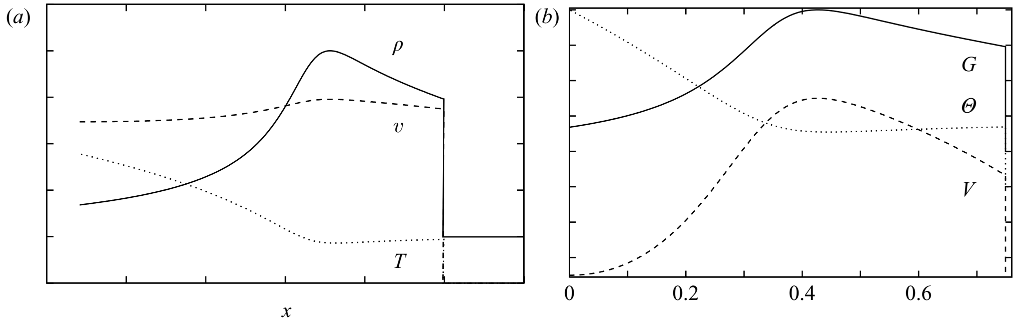

FIGURE 5. Structure of a self-similar flow in the case of a soft density gradient, $\left(\mathscr{B}_\varphi = 0.26, \mathscr{B}_p = 0.92, \gamma = 5/3\right)$. Density ρ, temperature T and velocity v are represented (*a*) *vs*. space at a given time, (*b*) by their reduced functions G, Θ and V. Note that the temperature of the fluid at rest is equal to zero.

3.1. *Chart* $\left(\mathscr{B}_\varphi, \mathscr{B}_p, \gamma = 5/3\right)$

As already said, there is a duality between the physical quantities $(\mathscr{B}_\varphi, \mathscr{B}_p)$, which stipulate the boundary conditions at the origin, and the numerical parameters (ξ_f, ξ_s), which define the locations of the origin and the end of the shocked-fluid zone, respectively. The numerical solution starts with the latter quantities whereas the definition of an experimental configuration deals with the former. It is then of interest to build a chart establishing the relationship between both types of quantities. Such a chart, built from about 300 flows, is represented in figure 6 for electron heat conduction and an adiabatic exponent $\gamma = 5/3$. Thus for a particular experimental configuration, characterized by the two boundary conditions $(\mathscr{B}_\varphi, \mathscr{B}_p)$, we readily obtain the numerical parameter values (ξ_f, ξ_s). The black lines correspond to constant values of the shock-wave locations, ξ_s, and red lines correspond to constant values of ξ_f, the location of the origin of the shocked-fluid zone. Three regions can be observed in this figure. First, a region where the lines with constant values of ξ_s are horizontal, i.e., do not depend on the value of $\mathscr{B}_\varphi$. In other words, varying the heat flux at the origin only changes, at least in this region, the location of the ablation front. Then a transition region, where both values $(\mathscr{B}_\varphi, \mathscr{B}_p)$ vary and an asymptotic region where maximal values of $\mathscr{B}_\varphi$ are reached. We have also plotted the straight line '$V(\xi = 0) = 0$' in this chart. Flows located on the right-hand side of this line are characterized by a negative velocity at the origin and flows located on the left-hand side have a positive value at the origin. The smaller the velocity at the origin, the larger the expansion wave. Obviously, the larger the expansion wave, the smaller the density at the origin and the steeper the ablation front. This type of solution occurs if the pressure at the boundary is not too large. Notice that the blue and green diamonds correspond to the flows displayed in figures 4 and 5, respectively. They illustrate the previous remarks. In figure 4, the self-similar solution describes a strong expansion wave. In such a case, the density at the origin is close to zero. An opposite case is provided in figure 5 where the velocity at the origin is close to zero, the expansion wave is weaker and the ablation front density gradient is softer. This is the case when the boundary pressure is large with respect to the value of the heat flux $\mathscr{B}_\varphi$.

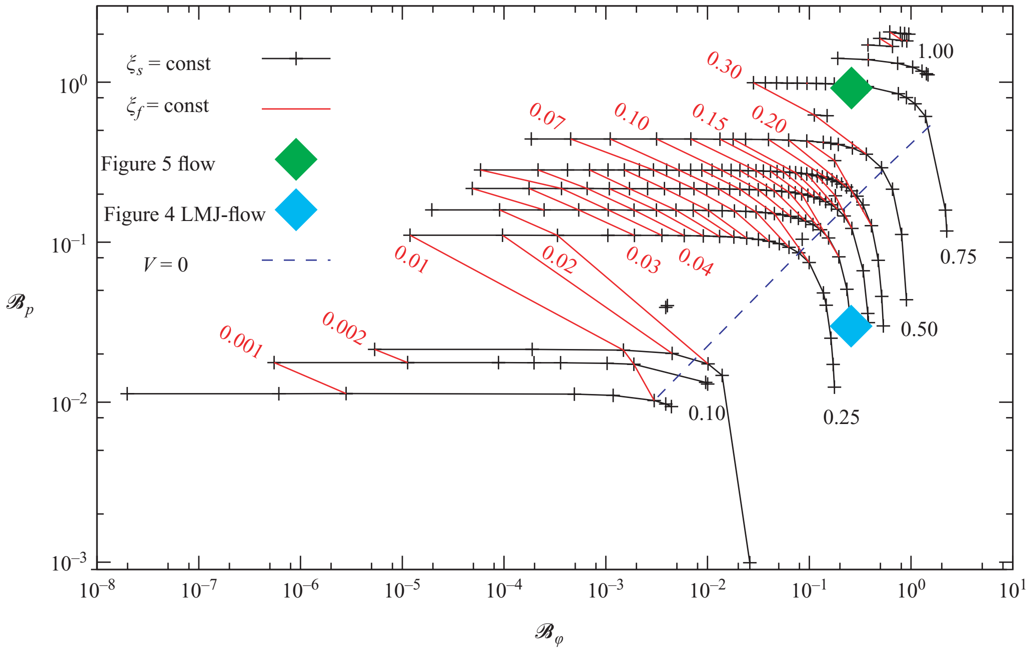

FIGURE 6. A chart relating the parameters ($\mathscr{B}_\varphi$, $\mathscr{B}_p$) and (ξ_f, ξ_s), allowing us to determine the starting point of a numerical solution (ξ_f, ξ_s), knowing the physical boundary conditions ($\mathscr{B}_\varphi$, $\mathscr{B}_p$). This chart has been built from more than 300 self-similar solutions for electron heat conduction $\nu = 5/2$ and an adiabatic exponent $\gamma = 5/3$. Three regions may be distinguished: a region where the lines with constant values for ξ_s are horizontal, then a transition region, where both values ($\mathscr{B}_\varphi$, $\mathscr{B}_p$) vary and an asymptotic region where the maximal values of $\mathscr{B}_\varphi$ are reached. The straight line defined by '$V(\xi = 0) = 0$' separates solutions characterized by negative (right-hand side) and positive (left-hand side) values of the velocity at the origin $V(\xi = 0)$.

4. Physical analysis

Here, we start by defining the dimensionless numbers which characterize the self-similar flows. Then two sub-families obtained by varying the pressure at the boundary $\mathscr{B}_p$ and the adiabatic exponent γ, are analysed in terms of these numbers in detail.

4.1. *Dimensionless numbers*

Length, velocity and acceleration

Several length scales may be defined in order to characterize the present deflagration flows. All these length scales have the following form: $\ell(m, t) = t^\alpha L(\xi)$, where ℓ is a length and L the associated reduced function. It is natural in such a problem to use a local length scale based on the temperature gradient

$$\ell_T(m,t) \equiv \left| \frac{1}{T(m,t)} \frac{\partial T}{\partial x}(m,t) \right|^{-1} = \left| \frac{\rho(m,t)}{T(m,t)} \frac{\partial T}{\partial m}(m,t) \right|^{-1}$$
$$= t^\alpha \frac{\Theta(\xi)}{G(\xi)} \left| \frac{\mathrm{d}\Theta(\xi)}{\mathrm{d}\xi} \right|^{-1} \equiv t^\alpha L_T(\xi). \tag{4.1}$$

This length scale depends on the self-similar coordinate ξ. We then choose to use a global length scale, namely the value of L_T at the point ξ_T where the temperature-gradient length scale is minimal. This abscissa ξ_T also defines the location of the ablation front. Thus there are three different remarkable points, whose locations are close to each other, but with different meanings. The first one is the location of the maximum density, ξ_a, the second is the origin of the shocked-fluid zone, ξ_f, and the third is the location of the ablation front, ξ_T, defined above. We also need a transformation formula between the ξ- and the (x,t)-spaces. For a given value of ξ, say ξ_*, we deduce the corresponding abscissa x of the point of Lagrangian coordinate $m = \xi_* t^\alpha$ through

$$x(m,t) = x(\xi_*\, t^\alpha, t) = \frac{t^\alpha}{\alpha}\left(\frac{\alpha\,\xi_*}{G(\xi_*)} + V(\xi_*)\right) + x(0,0). \tag{4.2}$$

Equation (4.2) has been used to plot figures 4(a) and 5(a) from figures 4(b) and 5(b) with $x(0,0) = 0$. The fluid velocity relative to the ablation front, defined by the location ξ_T, is

$$\begin{aligned} v'_x(m,t) &\equiv v(m,t) - \left(\frac{\partial x}{\partial t}(m = \xi\, t^\alpha, t)\right)_{\xi_T} \\ &= t^{\alpha-1}\left(V(\xi) - V(\xi_T) - \frac{\alpha\,\xi_T}{G(\xi_T)}\right) \equiv t^{\alpha-1}V'(\xi). \end{aligned} \tag{4.3}$$

The acceleration $a_x(m,t)$ is

$$a_x(m,t) \equiv \frac{\partial}{\partial t} v_x(m,t) = \frac{\partial}{\partial t}\left(t^{\alpha-1}V\right) = t^{\alpha-2}\left((\alpha-1)V - \alpha\,\xi\frac{\mathrm{d}V}{\mathrm{d}\xi}\right) \equiv t^{\alpha-2}A(\xi), \tag{4.4}$$

while the ablation front acceleration in the laboratory reference frame is given by

$$\begin{aligned} a'_x(t) &\equiv \left(\frac{\partial^2 x}{\partial t^2}(m = \xi\, t^\alpha, t)\right)_{\xi_T} \\ &= (\alpha-1)t^{\alpha-2}\left(V(\xi_T) + \frac{\alpha\,\xi_T}{G(\xi_T)}\right) \equiv t^{\alpha-2}A'. \end{aligned} \tag{4.5}$$

Mach, Froude and Péclet numbers

The Mach number characterizes the compressibility of the flow. We first define a Mach number with respect to the laboratory reference frame, based on the isentropic sound speed c_S, $M = v_x/c_S$. This absolute Mach number M_{abs} is

$$M_{abs}(\xi) = \frac{|V(\xi)|}{\sqrt{\gamma\,\Theta(\xi)}}. \tag{4.6}$$

Figure 7 represents the Mach number M_{abs} at the point ξ_a where the maximum density is reached. This absolute Mach number value depends essentially on the heat flux at the boundary $\mathscr{B}_\varphi$, according to the power law

$$M_{abs}(\xi_a)|_{(\mathscr{B}_\varphi,\mathscr{B}_p,\gamma)} \approx C_{f1}(\gamma) \times \mathscr{B}_\varphi^{C_{f2}(\gamma)}, \tag{4.7}$$

with $C_{f1}(\gamma = 5/3) = 1.44092$ and $C_{f2}(\gamma = 5/3) = -0.0484176$. This kind of dependence is also observed for other values of the exponent γ. A second Mach number is defined based on the velocity relative to the ablation front, namely

$$M(\xi) = \frac{|V'(\xi)|}{\sqrt{\gamma\,\Theta(\xi)}}. \tag{4.8}$$

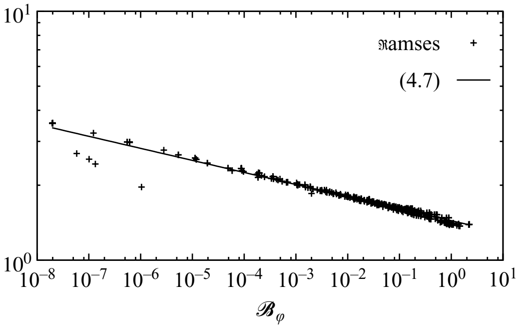

FIGURE 7. Absolute Mach number values at the point where the maximum density is reached: $M_{abs}(\xi_a)$ *vs.* $\mathscr{B}_\varphi$, for $\gamma = 5/3$ and about 300 values of $\mathscr{B}_p$ (symbols). The Mach number dependency on the boundary heat flux $\mathscr{B}_\varphi$ is also shown (line). Similar dependencies are observed for different values of γ.

The Froude number, $Fr = v/\sqrt{g\,\ell}$, which characterizes the relative importance of inertial effects with respect to acceleration effects, is

$$Fr(\xi) = \frac{V'(\xi)}{\sqrt{A'\,L(\xi)}}, \tag{4.9}$$

where the length scale L may be chosen between

the minimal temperature-gradient length scale

$$L_{\nabla T} \equiv L_T(\xi_T) = \min_{\xi} L_T(\xi), \tag{4.10}$$

the hot flow region length scale

$$L_{hot} = (x(\xi_T t^\alpha, t) - x(0, t))\, t^{-\alpha}, \tag{4.11}$$

the cold flow region length scale

$$L_{cold} = (x(\xi_s t^\alpha, t) - x(\xi_T t^\alpha, t))\, t^{-\alpha}. \tag{4.12}$$

The Péclet number, $Pe = \ell v/\chi$ with $\chi = \kappa/\rho\, C_p$, measuring the relative importance of heat convection over heat conduction effects, is

$$Pe(\xi) = \frac{\gamma}{\gamma - 1}\frac{L_{\nabla T}\, V'(\xi)}{G(\xi)^{-\mu-1}\,\Theta(\xi)^\nu}. \tag{4.13}$$

4.2. *Analysis of two sub-families*

For some insight into these self-similar ablative flow solutions, we have focused on two particular sub-families. The first one is obtained by varying the pressure at the boundary, i.e. $\mathscr{B}_p$, the second one by varying the compressibility of the fluid, i.e. the adiabatic exponent γ.

4.2.1. $\mathscr{B}_p$*-family for* $\left(\mathscr{B}_\varphi = 10^{-2}, \gamma = 5/3\right)$

For a given heat flux at the boundary $\mathscr{B}_\varphi$ and a fixed value of the fluid adiabatic exponent γ, we have plotted in figure 8 seven self-similar solutions for different values of $\mathscr{B}_p$, ranging from 10^{-2} to 0.4. Note that both the location of the shock wave ξ_s and the size of the shocked-fluid region grow with the pressure at the boundary, $\mathscr{B}_p$. The value of the density G at the shock wave appears to be constant. This value is given by (A2), and, for a small heat flux, depends essentially on the exponent

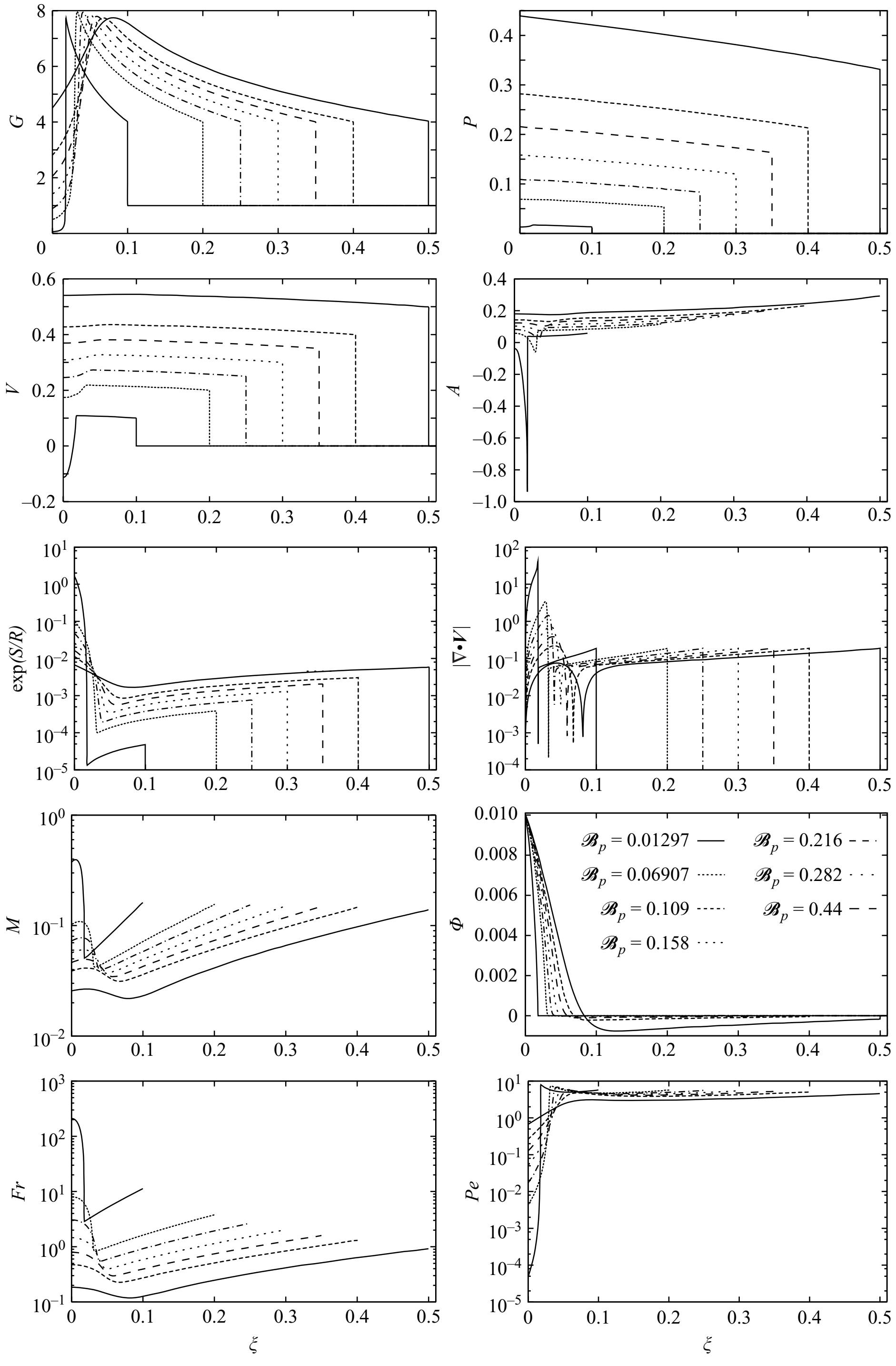

FIGURE 8. Reduced functions of the $\mathscr{B}_p$-family for $\left(\mathscr{B}_\varphi = 10^{-2}, \gamma = 5/3\right)$ and seven values of $\mathscr{B}_p$. From top to bottom and left to right, we have plotted the density G, pressure P, velocity V, acceleration A, entropy $\exp(S/R)$, norm of the divergence of the velocity $|\nabla\cdot V|$, Mach number M, heat flux Φ, Froude number Fr and Péclet number Pe *vs*. the ξ-abcissa. See text for comments.

γ. The maximal value reached by the density, in the vicinity of the ablation front, varies slightly (from 7.7 to 8) and the density gradient in the ablation zone becomes steeper as the value of the pressure $\mathscr{B}_p$ becomes smaller. The value of the pressure P undergoes moderate variations in the ξ-space and is close to a straight line at least for the highest values of $\mathscr{B}_p$. The order of magnitude of the pressure is given either by its value at the shock wave (A2) or by the value of $\mathscr{B}_p$.

In the same way, the velocity V varies slightly, except for small values of $\mathscr{B}_p$, its level is given by (A2): $V(\xi_s) \approx 2\alpha\,\xi_s/(\gamma+1)$. The smaller the velocity value at the boundary $\xi = 0$, the larger the expansion wave. Using (2.11*b*) and (4.4), we obtain $\mathrm{d}P/\mathrm{d}\xi = -A$. Acceleration profiles are flat for large values of $\mathscr{B}_p$. As the boundary pressure decreases, a bump appears in the ablation zone which turns into a peak for the smallest value of $\mathscr{B}_p$. Hence pressure profiles in the conduction zone are not as flat as the graphs suggest. We also note that the larger the value of $\mathscr{B}_p$, the faster the shock wave and the weaker the gradients in the ablation zone.

We have also drawn in figure 8 the Kovásznay modes (Chu & Kovásznay 1957), namely the entropy and the divergence of the velocity (there is no vorticity in such one-dimensional flows). The smaller the pressure $\mathscr{B}_p$ at the boundary, the steeper the entropy variation in the ablation zone. We also remark that the entropy is not uniform in the shocked-fluid region and the heat conduction is negligeable. The divergence of the velocity $\nabla\cdot V$ is proportional to the gradient of density, according to (2.11*a*): $\mathrm{d}V/\mathrm{d}\xi = (\alpha\xi/G^2)\mathrm{d}G/\mathrm{d}\xi$. It is seen to be negative and small in the shocked-fluid region (which corresponds to an increasing density, from the shock wave to the ablation front), and to reach its largest positive value in the ablation zone (which corresponds to a strong density gradient in the expansion wave). The maximal value of the velocity divergence increases when the value of the boundary pressure $\mathscr{B}_p$ decreases.

The maximal Mach-number value is reached at the shock-wave front, except for the smaller value of $\mathscr{B}_p$. Its minimal value is observed in the ablation zone and decreases when $\mathscr{B}_p$ increases. The same behaviour is observed with the Mach-number value at the origin. Recall that the heat flux is strongly positive in the ablation zone, and slightly negative in the shocked-fluid region. The temperature gradient length scale $L_{\nabla T}$, used to estimate the Froude and Péclet numbers, calculated with (4.1) is, in most cases, of the order of 10^{-3}, but may reach 10^{-5} for small values of $\mathscr{B}_p$. It is worth noting that the Chebyshev numerical method is able to describe solutions for which the ratio of length scales $L_{\nabla T}G(\xi_T)/\xi_s$ is of the order of 10^{-3}. The Froude number reaches its minimal values in space in the ablation zone. The steeper the Froude number profile in the ablation zone, the smaller the pressure and the velocity at the origin. The Péclet number reaches its maximal value – although it is not very large – in the shocked-fluid region, which is dominated by convection effects.

4.2.2. γ-*family for* $\left(\mathscr{B}_\varphi = 10^{-2}, \mathscr{B}_p = 10^{-1}\right)$

We have plotted in figure 9 five self-similar solutions for different values of the adiabatic exponent γ between 1.38 and 2, and for given pressure and heat flux boundary conditions $\mathscr{B}_p$ and $\mathscr{B}_\varphi$. We notice that the shock-wave location ξ_s increases with the exponent γ, while the size of the shocked-fluid region decreases. The value of the density G at the shock wave decreases when γ grows (from 6.3 to 3). This value is approximately given by (A2) and depends essentially on the value of γ. The maximal value of the density, reached in the ablation zone, strongly decreases when γ grows (from 16 to 5). The smaller the value of γ, the steeper the density gradient in the ablation zone. The value of the temperature Θ at $\xi = 0$ varies slightly. On the other

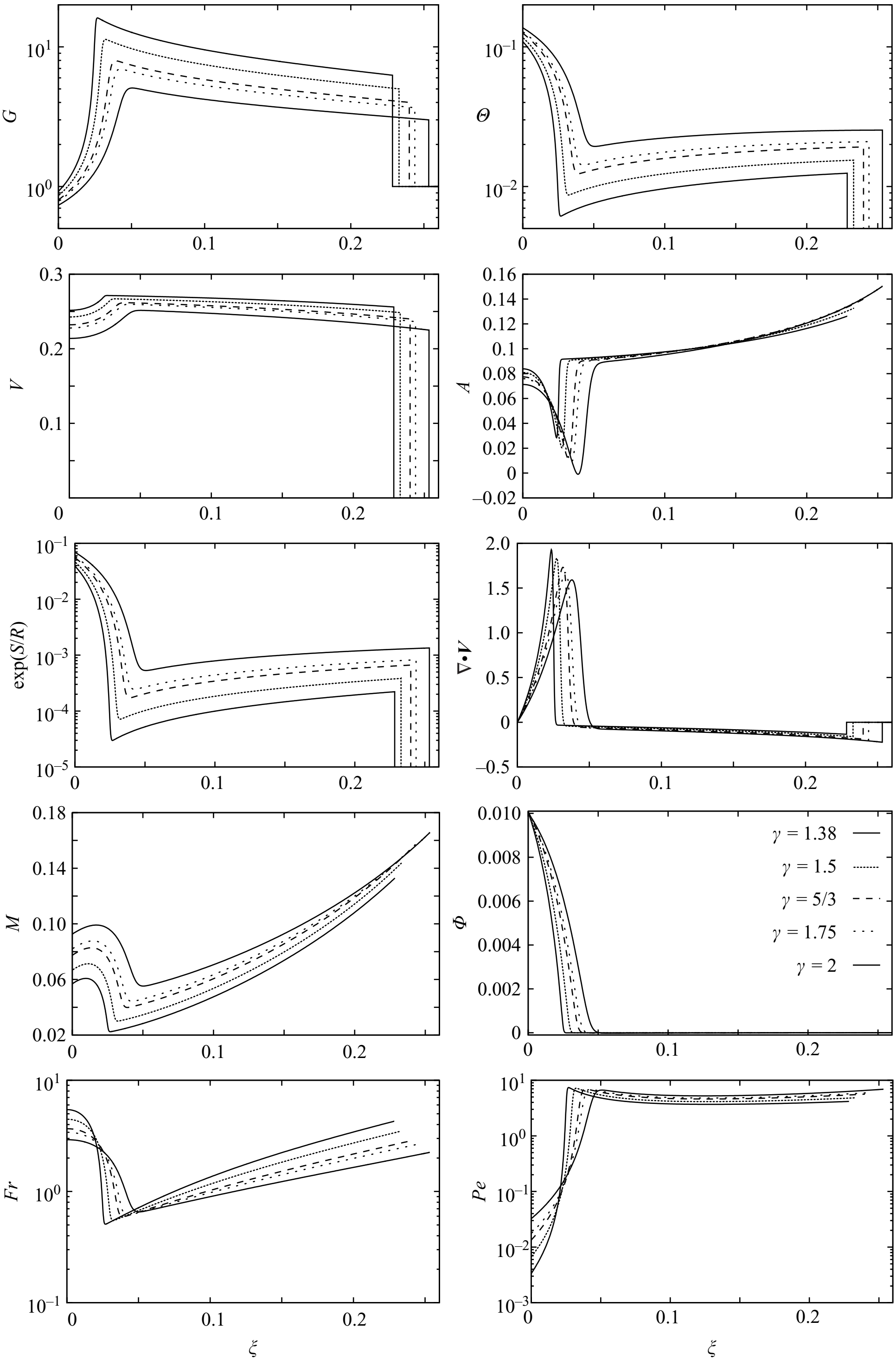

FIGURE 9. Reduced functions of the γ-family for $\left(\mathscr{B}_\varphi = 10^{-2}, \mathscr{B}_p = 10^{-1}\right)$ and five values of γ. From top to bottom and left to right, we have plotted the density G, temperature Θ, velocity V, acceleration A, entropy $\exp(S/R)$, divergence of the velocity $\nabla\cdot V$, Mach number M, heat flux Φ, Froude number Fr and Péclet number Pe *vs*. the ξ-abscissa. See text for comments.

hand, its value at the shock wave increases with γ and can be estimated from (A2). We then deduce that ξ_s grows faster than $\sqrt{\gamma - 1}$. The temperature difference between the hot flow and the shocked-fluid region $(\Theta(0) - \Theta(\xi_s))$ diminishes when the adiabatic exponent γ grows. The more compressible the fluid, the smaller the temperature jump at the shock wave. The overall energy available to expand the fluid is then larger, resulting in stronger density jumps between the ablation zone and the vicinity of the origin. We also note that, the smaller the adiabatic exponent γ, the larger the gradients of physical quantities (density, temperature, heat flux, entropy and Mach number). Regarding the velocity V, its global level slightly increases as γ decreases, as indicated by (A2): the fluid velocity at the shock wave $(V(\xi_s) \approx 2\alpha\xi_s/(\gamma + 1))$ increases when γ decreases.

As in figure 8, we have also drawn in figure 9 the Kovásznay modes (Chu & Kovásznay 1957). The entropy behaves as the temperature, although the density strongly decreases across the expansion wave. The divergence of the velocity is negative and small in the shocked-fluid zone and positive and large in the ablation zone. Thus the fluid is slightly compressed from the shock wave to the ablation front, and strongly expanded afterward.

The minimal Mach-number value in space is reached in the ablation zone, its maximal value at the shock wave front. The Mach number increases with the exponent γ. Increasing the adiabatic exponent without changing the pressure at the origin increases the pressure at the shock front and the pressure gradient between the origin and the shock. The Froude number reaches its minimal value in the ξ-space in the ablation zone. This value increases as the flow becomes more incompressible. Once again, the effects of acceleration are relatively small. As already mentioned, the Péclet number reaches its maximal value in the shocked-fluid region.

5. Application to ICF flows: the low-Mach-number approximation

As already stated in §1, most of the ablative mean flow models which have been built and the corresponding stability analyses which have been carried out, in the context of ablative RT or RM-instabilies in ICF, rely on a low-velocity hypothesis. The underlying approximation is actually the 'Low Mach number approximation' (LM) previously developed within the framework of natural convection (Paolucci 1982). A simple argument of asymptotic analysis provides three inequalities that guarantee the validity of the LM approximation, namely

$$\gamma M^2 \ll 1, \qquad Fr \gg \sqrt{\gamma M^2}, \qquad Pe \gg \gamma M^2, \qquad (5.1a, b, c)$$

where M is a Mach number. In the context of ICF ablative flows, this approximation was first used by Kull & Anisimov (1986) who developed a model for ablation fronts in steady mean flows subject to an acceleration field. A hydrodynamical stability analysis based on this ablation-flow model was subsequently performed by Kull (1989). Within this model, ablative flows are essentially characterized by a single dimensionless parameter $\Gamma = g\kappa/v^3$ defined in terms of the thermal diffusivity and the fluid velocity relative to the ablation front – 'ablation velocity'. In this analysis, the subsonic character of three ablation flows was checked, while the parameter Γ, which is also written $\Gamma = 1/(Fr^2\, Pe)$, was found to be in the range [1, 4]. Bychkov, Golberg & Liberman (1994) also considered the stability of such flows, assuming that the two constraints (5.1a) and (5.1b) were fulfilled although without actually performing any check against numerical simulations or experiments. The same hypotheses, (5.1a)

and (5.1*b*), were also used in the asymptotic analyses of the ablation front stability problem undertaken in a series of papers starting with Goncharov *et al.* (1996). Such assumptions were justified based on the claim that for realistic ICF pellet implosions, the Mach number at the ablation surface is much smaller than unity and the fluid stratification, within the density gradient length scale, is negligible. The same approximation is also used by Piriz, Sanz & Ibañez (1997) to study discontinuous ablation fronts. Clavin & Masse (2004) made a comparison of instabilities in ablation front and flames by equally assuming that criteria (5.1*a*) and (5.1*b*) were satisfied. Hence since this quasi-incompressible model is widely used for stability analyses of ablation fronts, it is worth checking whether or not the present self-similar solutions may fit an LM description. This analysis is performed on the whole sub-family of self-similar solutions detailed above (figure 6). Let us recall that one of these solutions – or one region of the plane $(\mathscr{B}_\varphi, \mathscr{B}_p)$ – is representative of the flows that could be achieved with the LMJ laser. We first derive the three inequalities which guarantee the validity of the LM approximation. The basic idea of this approximation is to perform an asymptotic expansion in terms of a small parameter and to retain only the first two orders. To this end, the Euler equations with nonlinear conduction (2.2) are rewritten in the non-inertial reference frame attached to the ablation front. In this new frame, the fluid velocity becomes $v'_x = v_x - w_x(\xi_T, t)$, where $w_x(\xi_T, t)$ denotes the front velocity in the laboratory frame, whereas an inertial acceleration $g(t) \equiv \dot{w}_x(\xi_T, t)$ appears in the momentum and energy equations. In a second step, the system is written in a dimensionless form with the following units: ℓ for the length, v_{rel} for the velocity (relative to the ablation front), ρ_r for the density and T_r for the temperature. We obtain

$$\left.\begin{aligned}
&\frac{\partial}{\partial t}\left(\frac{1}{\rho}\right) - \frac{\partial v'_x}{\partial m} = 0,\\
&\frac{\partial}{\partial t}\left(v'_x\right) + \frac{1}{\gamma M^2}\frac{\partial p}{\partial m} + \frac{g}{Fr^2} = 0,\\
&\frac{\partial}{\partial t}\left(\frac{1}{2}{v'_x}^2 + \frac{1}{\gamma M^2}\mathscr{E}\right) + \frac{\partial}{\partial m}\left(\frac{1}{\gamma M^2}\, p\, v'_x + \frac{1}{\gamma M^2}\frac{\gamma}{(\gamma-1)\,Pe}\varphi_x\right) + \frac{g\, v'_x}{Fr^2} = 0.
\end{aligned}\right\} \tag{5.2}$$

The Mach (M), Froude (Fr) and Péclet (Pe), dimensionless parameters are thus defined as

$$M = \frac{v_{rel}}{\sqrt{\gamma\, R\, T_r}}, \qquad Fr = \frac{v_{rel}}{\sqrt{\tilde{g}\,\ell}}, \qquad Pe = \frac{\gamma}{\gamma-1}\,\frac{v_{rel}\,\ell}{\kappa_o/(\rho_r\, R)}, \tag{5.3}$$

where $\tilde{g}$ is a mean value of $g(t)$. A formal asymptotic expansion is performed by assuming

$$\phi = \phi^{(0)} + \gamma M^2\, \phi^{(1)} + (\gamma M^2)^2\, \phi^{(2)}, \tag{5.4}$$

for $\phi = \rho$, p, v'_x and $\mathscr{E}$. The continuity equation still holds for the zero-order quantities $\rho^{(0)}$ and $v'^{(0)}_x$. At the lowest order and first order, the momentum equation leads to

$$\frac{\partial p^{(0)}}{\partial m} = 0, \quad \frac{\partial}{\partial t} v'^{(0)}_x + \frac{\partial p^{(1)}}{\partial m} + \frac{g}{Fr^2} = 0, \tag{5.5a,b}$$

provided the Froude number is not too small, i.e. $\gamma\, M^2 \ll Fr^2$. In such a way, the third term of (5.5*b*) is a first-order term. At the same order, the energy equation is

$$\frac{\partial}{\partial t}\mathscr{E}^{(0)} + p^{(0)}\frac{\partial}{\partial m}\left(v'^{(0)}_x + \frac{\gamma}{(\gamma-1)\,Pe}\varphi^{(0)}_x\right) = 0, \tag{5.6}$$

provided the Péclet number is not too small, i.e. $\gamma M^2 \ll Pe(\gamma-1)/\gamma$. As a result, a flow satisfying the three constraints

$$\gamma M^2 \ll 1, \qquad \frac{\gamma M^2}{Fr^2} \ll 1, \qquad \frac{\gamma}{\gamma-1}\frac{\gamma M^2}{Pe} \ll 1, \qquad (5.7a,b,c)$$

may be approximated by a set of equations in which acoustic waves are no longer solutions. In other words, the hyperbolic part of the Euler equations (2.2) or (5.2) has been removed, the resulting set of equations being close to the incompressible flow equations although some density variations are allowed. The next step of this analysis is to explicitly calculate (5.7). The first criterion (5.7*a*) simply means that the velocity has to be small with respect to the sound velocity, i.e. that the acoustic part of the flow is small. The second criterion (5.7*b*) may be rewritten by means of the formula

$$\frac{\gamma M^2}{Fr^2} = \frac{\gamma V'^2}{\gamma P/G}\frac{A'\,L}{V'^2} = \gamma\,\frac{A'\,L}{C_S^2}, \qquad (5.8)$$

where C_S is the isentropic sound speed. This criterion will be satisfied as long as the acceleration and the characteristic length scale are not too large and the sound speed is large enough. Note that (5.8) is also the ratio of a characteristic length, $\mathscr{L}$, over the 'scale height' of the fluid $C_S^2/\gamma A'$, and is therefore a measure of the fluid stratification. Consequently, several length scales may be considered, depending on the flow region under study. Given the self-similar ablative flow structure (figure 4), three different length scales naturally arise: the temperature gradient length scale $L_{\nabla T}$ of (4.10), and the lengths of the hot (L_{hot}) and cold (L_{cold}) flow regions as given by (4.11) and (4.12), respectively. To each of these length scales corresponds a Froude number (4.9) and a stratification measure (5.8) of the relevant portion of the flow, namely

$$\frac{\gamma M^2}{Fr_T^2} = \gamma\,\frac{A'\,L_{\nabla T}}{C_S^2}, \qquad \frac{\gamma M^2}{Fr_{hot}^2} = \gamma\,\frac{A' L_{hot}}{C_S^2}, \qquad \frac{\gamma M^2}{Fr_{cold}^2} = \gamma\,\frac{A' L_{cold}}{C_S^2}. \qquad (5.9a,b,c)$$

Within the framework of ablation front stability studies, authors have typically used a length scale, L_0, based on the heat conduction coefficient and the ablation velocity (Betti *et al.* 1996). They also define the density gradient length scale, L_m with $L_m \approx 8L_0$ for $\nu = 5/2$. The criterion (5.7*b*), (5.9*a*) is more easily satisfied with such a definition of length scale L_0, since L_m is very close to the temperature gradient length scale, $L_{\nabla T}$. However, the LM approximation requires that the flow stratification be weak. It is therefore necessary to evaluate the stratification of each of the characteristic regions of an ablative flow in order to assess the relevance of the LM approximation. This leads us to consider the three constraints made of (5.7*b*) with the definitions of (5.9). The third criterion (5.7*c*) may be expressed as the ratio of an atom collision time scale to a hydrodynamic time scale, thus assessing the validity of the hydrodynamic approximation.

Values of the four LM criteria have been represented in the plane $(\mathscr{B}_\varphi, \mathscr{B}_p)$ in figure 10, where the maximum over the space variable ξ has been taken: γM^2, the stratification of the hot part of the flow $\gamma M^2/Fr_{hot}^2$, of the cold part $\gamma M^2/Fr_{cold}^2$ and the hydrodynamic constraint $\gamma/(\gamma-1)\,\gamma\,M^2/Pe$. Numerical values have been rescaled with the function $\mathsf{F}(q) = \tanh(2\log q)$ in order to bring them in the interval $[-1,+1]$. It appears that, for large heat fluxes and moderate pressures at the boundary, the self-similar solutions do not satisfy the first LM criterion (5.7*a*), which

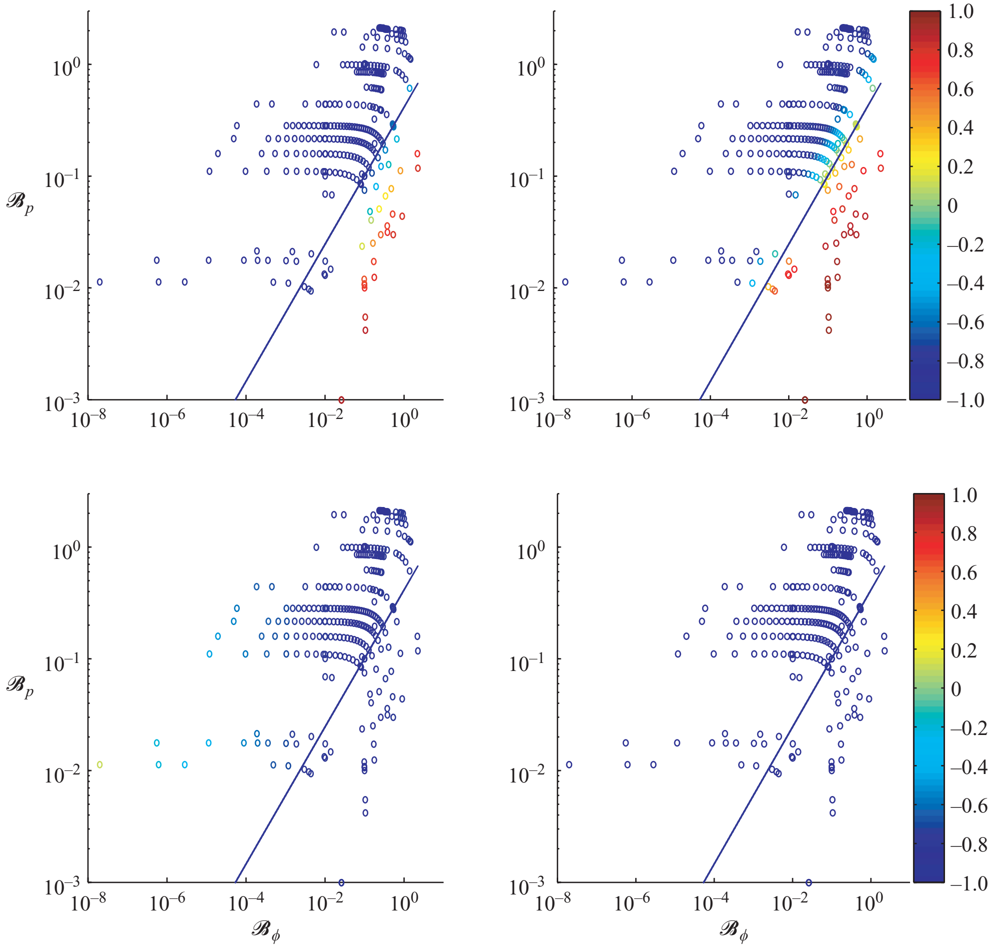

FIGURE 10. Plots of the maximum values in ξ of the ratios entering the four low-Mach-number criteria (5.7*a*), (5.7*b*) with (5.9*b*) or (5.9*c*), and (5.7*c*), in the plane $(\mathscr{B}_\varphi, \mathscr{B}_p)$ for the set of self-similar solutions of figure 6 (where $\mu = 0$, $\nu = 5/2$ and $\gamma = 5/3$). (*a*) γM^2; (*b*) $\gamma M^2/\mathrm{Fr}^2_{hot}$, (*c*) $\gamma M^2/\mathrm{Fr}^2_{cold}$, (*d*) $\gamma/(\gamma - 1)\gamma M^2/Pe$. Ratio data have been mapped with the transform function $\mathsf{F}(q) = \tanh(2 \log q)$ to make an easier reading of the results: the colour chart ranges from blue ($\mathsf{F}(q) \to -1$) for the lowest values of the criteria ($q \to 0$) to red ($\mathsf{F}(q) \to 1$) for the largest values ($q \to \infty$) while values close to unity ($q \approx 1$) appear in green ($\mathsf{F}(q) \approx 0$). The first criterion, (5.7*a*), is seen to be satisfied for solutions on the upper-left-hand side of the line '$V(\xi = 0) = 0$' in the $(\mathscr{B}_\varphi, \mathscr{B}_p)$-plane. The second criterion (5.7*b*), with (5.9*b*), is somewhat similar in behaviour. The third criterion, (5.7*b*) with (5.9*c*), is verified except for the lowest levels of the boundary heat flux. The fourth criterion, (5.7*c*), holds for all the solutions tested.

characterizes the acoustic part of the flow. These solutions are located on the right-hand side of the straight line '$V(\xi = 0) = 0$' which separates solutions characterized by a negative and positive values of the velocity at the origin (see figure 6). The LMJ solution of figure 4 belongs to this region of the chart. However solutions obtained either with a small heat flux or a large pressure at the origin satisfy this criterion. The second criterion, (5.7*b*) with (5.9*b*), displays a similar behaviour: the straight line '$V(\xi = 0) = 0$' discriminates solutions with a strongly stratified hot-flow region (on the lower-right-hand side of the line) from those with a weakly stratified hot region (on the upper-left-hand side of the line). The third criterion in terms of (5.9*c*) shows that the stratification of the cold region is always negligible, even for solutions in the LMJ energy range. Criterion (5.7*b*) with (5.9*a*) has been found to be satisfied (not shown here) for all the solutions of the chart in figure 6. The same conclusion holds for the criterion approximation based on the Péclet number, (5.7*c*) hereby meaning that the hydrodynamic hypothesis is valid for all the investigated self-similar flows. In particular, solutions studied in § 4.2.1 (figure 8) mostly satisfy the five criteria (5.7) with (5.9), except for the solution with the smallest value of $\mathscr{B}_p$.

As a result, self-similar ablation flows obtained within the framework of the present hypotheses (electron heat conduction, growing heat flux at the boundary, etc.) for large heat fluxes and not too large pressures at the boundary do not satisfy the low-Mach-number approximation criteria. This is, in particular, the case for deflagration density-invariant self-similar solutions obtained for energies in the range of the LMJ facility. Such flows cannot be approximated by the low-Mach-number approximation, i.e. by means of a stationary quasi-incompressible flow. As a result, we must check stratification criteria (5.9) in each region of an ablation flow prior to the use of the LM approximation, including for flows relevant to the acceleration phase in ICF.

6. Conclusion

We have detailed some properties of self-similar solutions for inviscid compressible ablative flows in slab symmetry with nonlinear heat conduction relevant to inertial confinement fusion. A sophisticated and reliable auto-adaptive Chebyshev multidomain method has been devised in order to solve the nonlinear eigenvalue problem resulting from the application of the two-parameter Lie group symmetry. A sub-family which leaves the density invariant is detailed since these solutions may be used to model the ‘early-time’ period of an ICF-implosion where a shock wave travels from the front to the rear surface of the target. A physical analysis of these unsteady ablation flows has been provided where solutions are characterized by dimensionless numbers (Mach, Froude and Péclet numbers). In particular, a chart allowing us to determine the starting point of a numerical solution, knowing the physical boundary conditions, has been built with over 300 self-similar solutions. These solutions correspond to ablative flows of a monatomic gas ($\gamma = 5/3$) owing to electron heat conduction according to the Spitzer–Harm model (nonlinear heat conduction exponents $\mu = 0$ and $\nu = 5/2$; see Duderstadt & Moses 1982). These assumptions are characteristic of the ablation of a low-atomic-number material by a direct laser illumination – the so-called direct-drive scheme for ICF. Furthermore, an approximate scaling law, which connects the absolute Mach number of the flow at the ablation front, to the heat flux at the origin is given. These solutions are typically characterized by moderate Froude and Péclet numbers in the shocked-fluid region. We have also shown that self-similar ablation fronts generated within the framework of the present hypotheses (electron heat conduction, growing heat flux at the boundary, etc.) and for large heat fluxes and not too large pressures at the boundary do not satisfy the low-Mach-number criteria. This is, in particular, the case for self-similar solutions obtained for energies in the range of the Laser MegaJoule laser facility. Consequently these flows cannot be approximated by the low-Mach-number approximation, i.e. by means of a stationary quasi-incompressible flow, as is often assumed in inertial confinement fusion. The Mach numbers of these flows are not low enough and stratification of the hot region cannot be neglected.

Two particular solutions of this family have been used for studying stability properties of ablation flows (Abéguilé *et al.* 2006; Clarisse *et al.* 2006; Lombard *et al.* 2007). Solutions representative of various ablation flows (radiation heat wave, quasi-incompressible, etc.) could be modelled with such time-dependent solutions through variations of the fluid parameters, i.e. the exponents of the nonlinear heat conduction and of the equation of state. Investigation of such solutions is underway. Stability analyses based on these unsteady self-similar mean flows will be reported in detail in forthcoming papers.

We would like to acknowledge Messrs N. Salaün and A. Boutboul for having carried out parametric studies of self-similar solutions.

Appendix A. Rankine–Hugoniot jump relations

For the configuration of ablative flows in the deflagration regime, an isothermal shock wave penetrates the cold medium, followed by a thermal front. For a shock-compressed fluid region dominated by convection effects, as is the case here, the thickness of the isothermal shock wave is very small and the combination of the isothermal shock wave and the thermal front may be described by a perfect discontinuity (Marshak 1958). Within this approximation, the Rankine–Hugoniot conditions for a planar shock wave (Germain & Muller 1994) penetrating a cold medium at rest ($T = T_u = 0$) may be written as:

$$\left[\rho u_x\right]_D^U = 0, \tag{A1a}$$

$$\left[\rho u_x v_x - p\right]_D^U = 0, \tag{A1b}$$

$$\left[\left(\frac{p}{\gamma-1} + \frac{1}{2}\rho v_x^2\right) u_x - p v_x\right]_D^U + \varphi_{xD} = 0, \tag{A1c}$$

with the relation $u_x = w_x - v_x$, w_x being the front velocity in the chosen frame of reference. Downstream and upstream – with respect to the shock front – values of flow quantities are distinguished by, respectively, the subscripts D and U.

The mean-flow jump relations (A1) applied to the self-similar solution (2.9) with an upstream state given by $(G_U\ V_U\ P_U) \equiv (1\ 0\ 0)$, lead to (2.23) for the downstream values of the self-similar functions G, V and P. When omitting the downstream heat flux, φ_{xD}, we recover the classical Rankine–Hugoniot relations under the form

$$G_D = \frac{\gamma+1}{\gamma-1}, \quad V_D = \frac{2}{\gamma+1}W, \quad P_D = \frac{2}{\gamma+1}W^2, \tag{A2}$$

where the self-similar shock-front velocity is defined by (2.25).

Appendix B. Numerical method

The nonlinear eigenvalue problem (2.17) with the boundary conditions (2.21) and (2.22) is integrated with the following five stage numerical procedure (Boudesocque-Dubois 2000; Gauthier *et al.* 2005):

(*a*) *Backward finite-difference integration.* The boundary conditions (2.21) and the Rankine–Hugoniot relations without conduction (A2) give a starting value for $(G\ V\ \Theta)$ at ξ_s^-. Integrating (2.17) without heat conduction, by means of a Runge–Kutta scheme, from ξ_s^- to ξ_f^+ yields $\left(G(\xi_f^+)\ V(\xi_f^+)\ \Theta(\xi_f^+)\right)$, the values at ξ_f^- being evaluated by continuity, while $\Phi(\xi_f^-)$ is estimated with $\Phi(\xi_f^-) = -\left(G^{1-\mu}\Theta^{\nu}(\mathrm{d}\Theta/\mathrm{d}\xi)\right)(\xi_f^-)$. System (2.17) is then integrated from ξ_f^- to 0.

This way of proceeding provides a first guess at a solution which depends on the two parameters ξ_f and ξ_s – these parameters having to be adjusted for recovering the values (2.20) of $\mathscr{B}_p$ and $\mathscr{B}_\varphi$.

(*b*) *Forward finite-difference integration.* Starting with the estimate $\boldsymbol{Y}(0)$, system (2.17) is forward-integrated from 0 up to a certain point $\xi_{(?)}$. This point $\xi_{(?)}$ is adjusted to provide the best approximation of the Rankine–Hugoniot relations, measured by the absolute error on the values of $(G\ V\ \Theta)$ at the point ξ_s^+, $\boldsymbol{E}_{RH}$. The resulting value of $\xi_{(?)}$ defines a new value for the shock-wave front location ξ_s. This forward integration is stable and provides an approximation typically characterized by a relative error of the order of 10^{-3}.

(*c*) *Forward finite-difference integration on a multidomain spectral grid.* In order to obtain more accurate approximations, we choose to use a collocation spectral method (Peyret 2002). Consequently, we must obtain a numerical approximation of the solution on a spectral grid. In effect, the integration domain $[0, \xi_s]$ is decomposed into $\mathscr{N}$ contiguous subdomains $[a_i, b_i]$, $i = 1, \ldots, \mathscr{N}$, $a_1 = 0$, $b_{\mathscr{N}} = \xi_s$, of $\mathscr{N}_i$ collocation points defined by mapping the set of $\mathscr{N}_i$ Gauss–Lobatto collocation points with a coordinate transform (Gauthier *et al.* 2005).

The solution is thus estimated on this spectral grid with the previously used Runge–Kutta scheme. The subdomain interface locations and the mapping parameters are dynamically adapted by minimizing a norm of the computed solution (Renaud & Gauthier 1997).

(*d*) *Relaxation process.* The next stage consists in applying a relaxation method (Orszag 1980) to system (2.17) written under the form $\boldsymbol{L}\boldsymbol{Y} = \boldsymbol{f}$. The corresponding iterative method is written as

$$\boldsymbol{Y}^{(n+1)} = \boldsymbol{Y}^{(n)} - \mathsf{a}\boldsymbol{L}_{prec}^{-1}\left(\boldsymbol{L}_{sp}\boldsymbol{Y}^{(n)} - \boldsymbol{f}\right), \quad n \geqslant 0, \tag{B1}$$

with a chosen such that $0 < \mathsf{a} < 2/(m + M)$, where m and M are the smallest and the largest eigenvalue of $|\boldsymbol{L}_{prec}^{-1}\boldsymbol{L}_{sp}|$. The matrix $\boldsymbol{L}_{sp}$ is the Chebyshev approximation of the operator $\boldsymbol{L}$, and $\boldsymbol{L}_{prec}$ is the corresponding preconditioning operator, taken initially to be $\boldsymbol{L}_{sp}$ (Gauthier 1988). This last operator depends on the values of $\boldsymbol{Y}$, and its evaluation on each subdomain, at each iteration, is costly in terms of computational time. Therefore, $\boldsymbol{L}_{sp}^{-1}$ is evaluated only when the spectrum of $\boldsymbol{L}_{prec}^{-1}\boldsymbol{L}_{sp}$ becomes too wide. The above iterative process (B1) is applied on each subdomain, for increasing subdomain index, i.e. for increasing abscissa ξ. The first subdomain resolution includes the boundary conditions at $\xi = 0$. For the other subdomains, continuity of $\boldsymbol{Y}$ at each subdomain interface location is imposed. This iterative method gives a good estimate of the solution, the absolute error being close to machine precision (10^{-11} in our case), except around the subdomain interfaces where the error is about 100 times larger. However, the Rankine–Hugoniot relations are only satisfied with an error $\boldsymbol{E}_{\mathrm{RH}}$ of the order of 10^{-4}.

(*e*) *Boundary condition optimization.* In order to improve the approximation of the Rankine–Hugoniot relations, we introduce, as an ultimate stage, a recursive process for modifying the boundary condition value at the origin. This process amounts to the recursion

$$\boldsymbol{Y}|_{\xi=0}^{(n+1)} = \boldsymbol{Y}|_{\xi=0}^{(n)} + \boldsymbol{\epsilon} RH^{(n)}, \quad (n \geqslant 0), \tag{B2}$$

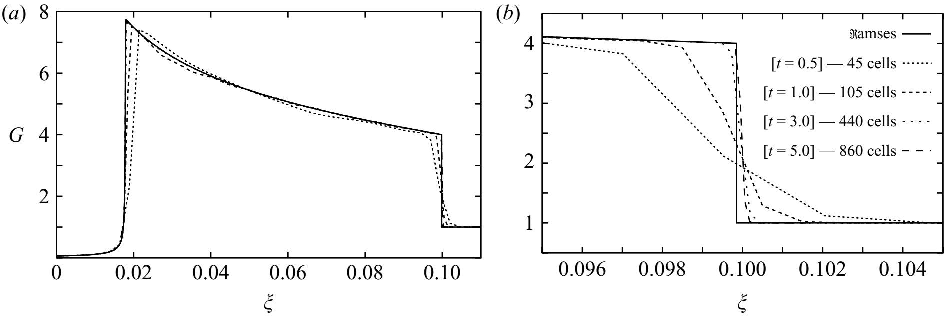

FIGURE 11. Global validation of the numerical method: comparison between the results computed by a Lagrangian finite-volume numerical method at different times (dashed lines) and the self-similar solution obtained with the spectral method (solid line). (*a*) The full density profiles and (*b*) the vicinity of the shock wave. The number of cells corresponding to the finite-volume computed solutions at each different time is also indicated.

where the free parameter $\boldsymbol{\epsilon}$ is a diagonal matrix, with diagonal elements taken in the interval $\left[0.2 \times 10^{-4}, 10^{-1}\right]$. This iterative process, while maintaining the same relative error level on the subdomains, allows us to divide the error $\boldsymbol{E}_{\mathrm{RH}}$ by a factor of 10.

The validation of the numerical method and the numerical code has been carried out in several ways. The main ingredients of the numerical method in stages (*a*)–(*c*) have been designed in order to obtain a sufficiently accurate guess for the relaxation process described in step (*d*). This relaxation process is routinely used for solving Helmholtz problems, with spectral or finite-difference preconditioning, which arise from implicit treatments of diffusive terms. An example of the convergence history of the relaxation process for the first-order differential operator and spectral preconditioning (B1) is provided in Gauthier *et al.* (2005).

The capability of this self-adaptive method has been checked on several fluid dynamics problems: (i) a one-dimensional initial- and boundary-value problem (IBVPs) – a rippled shock wave case – governed by Euler's equations and for which the exact solution is known; (ii) the stability analysis of the compressible Rayleigh-Taylor flow, governed by the Navier–Stokes equations, which reduces to a generalized linear eigenvalue problem; and (iii) several two-dimensional IBVPs – simulations of the Rayleigh–Bénard, Kelvin–Helmholtz and Rayleigh–Taylor flows (Renaud & Gauthier 1997; Gauthier *et al.* 2005; Lafay, Le Creurer & Gauthier 2007).

A global validation of the method has also been carried out in the present case by comparing spectral results with those obtained from a Lagrangian finite-volume method (Boudesocque-Dubois & Clarisse 2007). This latter method solves IBVPs for the Euler equations with nonlinear heat conduction (2.1)–(2.4), (2.15), (2.16), combining, through operator splitting, an explicit Godunov-type scheme for the hyperbolic part of the system, and an implicit-scheme for the complementary nonlinear parabolic equation. For illustrative purposes, a steep density gradient ablation flow has been retained: $\gamma = 5/3$, $\mathscr{B}_p = 0.01297$, $\mathscr{B}_\varphi = 0.01$ (see figure 8). The IBVP solution approximations provided at successive instants in time by the finite-volume method converge towards the self-similar solution spectral approximation (figure 11).

REFERENCES

ABÉGUILÉ, F., BOUDESOCQUE-DUBOIS, C., CLARISSE, J.-M., GAUTHIER, S. & SAILLARD, Y. 2006 Linear perturbation amplification in self-similar ablation flows of inertial confinement fusion. *Phys. Rev. Lett.* **97** (035002).

AGLITSKIY, Y., VELIKOVICH, A. L., KARASIK, M., SERLIN, V., PAWLEY, C. J., SCHMITT, A. J., OBENSCHAIN, S. P., GARDNER, A. N. MOSTOVYCH, J. H. & METZLER, N. 2002 Direct observation of mass oscillations due to ablative Richtmyer–Meshkov-like instability and feedout in planar plastic targets. *Phys. Plasmas* **9** (5).

ANISIMOV, S. I. 1970 Self-similar thermal wave in a two-temperature plasma heated by a laser pulse. *Sov. Phys., J. Exp. Theor. Phys. Lett.* **12**, 287–289.

ATZENI, S. & MEYER-TER-VEHN, J. 2004 *The Physics of Inertial Fusion*. Oxford University Press.

BAJAC, J. 1973 Étude d'une classe de solutions des écoulements plan compressibles avec transfert radiatif. Tech. Rep. CEA-R-4482. Commissariat à l'Énergie Atomique.

BARENBLATT, G. 1979 *Similarity, Self-Similarity and Intermediate Asymptotics*. Consultants Bureau, New-York.

BARRERO, A. & SANMARTÍN, J. R. 1977 Self-similar motion of laser fusion plasma. Absorption in an unbounded plasma. *Phys. Fluids* **20** (7), 1155–1163.

BETTI, R., GONCHAROV, V. N., MCCRORY, R. L., SOROTOKIN, P. & VERDON, C. P. 1996 Self-consistent stability analysis of ablation fronts in inertial confinement fusion. *Phys. Plasmas* **3** (5), 2122–2128.

BODNER, S. 1974 Rayleigh–Taylor instability and laser-pellet fusion. *Phys. Rev. Lett.* **33** (13).

BOUDESOCQUE-DUBOIS, C. 2000 Perturbations linéaires d'une solution autosemblable de l'hydrodynamique avec conduction non linéaire. PhD thesis, Université Paris 6.

BOUDESOCQUE-DUBOIS, C. & CLARISSE, J.-M. 2007 Traitement numérique des équations de la dynamique des gaz avec conduction non linéaire dans le code de perturbations silex. Tech. Rep. CEA-R-6137. Commissariat à l'Énergie Atomique.

BOUDESOCQUE-DUBOIS, C., CLARISSE, J.-M. & GAUTHIER, S. 2001 Hydrodynamic stability of ablation fronts: linear perturbation of a self-similar solution. In *ECLIM: 26th European Conf. on Laser Interaction with Matter* (ed. K. Rohlena, M. Kálal & M. Šiňor), *Proc. SPIE*, **4424**, 220–223.

BOUDESOCQUE-DUBOIS, C., GAUTHIER, S., CLARISSE, J.-M. & LOMBARD, V. 2006 Self-similar solutions of unsteady ablation flow. In *33rd EPS Conf. on Plasma Physics*, *ECA*, vol. 301.

BRUN, L., DAUTRAY, R., DELOBEAU, F., PATOU, C., PERROT, F., REISSE, J.-M., SITT, B. & WATTEAU, J.-P. 1977 Physical models and mathematical simulation of laser-driven implosion and their relations with experiments. In *Laser Interaction and Related Plasma Phenomena* (ed. H. J. Schwarz & H. Hora), vol. 4B, pp. 1059–1080. Plenum.

BYCHKOV, V. V., GOLBERG, S. M. & LIBERMAN, M. A. 1994 Self-consistent model of the Rayleigh–Taylor instability in ablatively accelerated laser plasma. *Phys. Plasmas* **1** (9), 2976–2986.

CHU, B.-T. & KOVÁSZNAY, L. 1957 Non-linear interactions in a viscous heat-conducting compressible gas. *J. Fluid Mech.* **3**, 494–514.

CLARISSE, J.-M., BOUDESOCQUE-DUBOIS, C., GAUTHIER, S. & ABÉGUILÉ, F. 2006 Linear perturbation amplification in ICF self-similar ablation flows. *J. Phys.* IV *France* **133**, 111–115.

CLAVIN, P. & MASSE, L. 2004 Instabilities of ablation fronts in inertial confinement fusion: a comparison with flames. *Phys. Fluids* **11** (2), 690–705.

DUDERSTADT, J. & MOSES, G. 1982 *Inertial Confinement Fusion*. Wiley-Interscience.

FORTIN, X. & CANAUD, B. 2000 Direct drive laser fusion calculations at cea. In *IFSA'99-Inertial Fusion Sciences and Applications, Bordeaux* (ed. Ch. Labaune, W. J. Hogan & K. A. Tanaka), pp. 102–105. Elsevier.

FRÖHLICH, J. & GAUTHIER, S. 1993 Numerical investigations from compressible to isobaric Rayleigh–Bénard convection in two dimensions. *Eur. J. Mech.* B/*Fluids* **12**, 141–159.

GAUTHIER, S. 1988 A spectral collocation method for two-dimensional compressible convection. *J. Comput. Phys.* **75**, 217–235.

GAUTHIER, S., LE CREURER, B., ABÉGUILÉ, F., BOUDESOCQUE-DUBOIS, C. & CLARISSE, J.-M. 2005 A self-adaptative domain decomposition method with Chebyshev method. *Intl J. Pure Appl. Maths* **24**, 553–577.

GERMAIN, P. & MULLER, P. 1994 *Introduction à la Mécanique des Milieux Continus*, 2nd edn. Masson, Paris.

GONCHAROV, V. N. 1999 Theory of the ablative Richtmyer–Meshkov instability. *Phys. Rev. Lett.* **82**, 2091–2094.

GONCHAROV, V. N., BETTI, R., MCCRORY, R. L., SOROTOKIN, P. & VERDON, C. P. 1996 Self-consistent stability analysis of ablation fronts with large Froude numbers. *Phys. Plasmas* **4**, 1402–1414.

Kull, H. J. 1989 Incompressible description of Rayleigh–Taylor instabilities in laser-ablated plasmas. *Phys. Fluids* B **1** (1), 170–182.

Kull, H. J. & Anisimov, S. I. 1986 Ablative stabilization in the incompressible Rayleigh–Taylor instability. *Phys. Fluids* **7** (29), 2067–2075.

Lafay, M.-A., Le Creurer, B. & Gauthier, S. 2007 Compressibility effects on the Rayleigh–Taylor instability growth between miscible fluids. *Europhys. Lett.* **79**, 64002.

Landau, L. D. & Lifchitz, E. M. 1987 *Fluid Mechanics*. Pergamon.

Le Métayer, O. & Saurel, R. 2006 Compressible exact solutions for one-dimensional laser ablation fronts. *J. Fluid Mech.* **561**, 465–475.

Lombard, V., Boudesocque-Dubois, C., Clarisse, J.-M. & Gauthier, S. 2007 Kovásznay modes in stability of self-similar ablation flows of ICF. In *34th EPS Conf. on Plasma Physics*, ECA, vol. 31F.

Majda, A. & Sethian, J. 1985 The derivation and numerical solution of the equations for zero Mach number combustion. *Combust. Sci. Technol.* **42**, 185–205.

Manheimer, W. & Colombant, D. 1982 Steady-state planar ablative flow. *Phys. Fluids* **25** (9).

Marshak, R. 1958 Effect of radiation on shock wave behavior. *Phys. Fluids* **1** (1), 24–29.

Moran, M. J. & Gaggioli, R. A. 1968 Reduction of the number of variables in systems of partial differential equations, with auxiliary conditions. *SIAM J. Appl. Maths* **16**, 202–215.

Murakami, M., Sakaiya, T. & Sanz, J. 2007 Self-similar ablative flow of nonstationary accelerating foil due to nonlinear heat conduction. *Phys. Plasmas* **14**, 022707.

Nuckolls, J., Wood, L., Thiessen, A. & Zimmerman, G. 1972 Laser compression of matter to super-high densities: thermonuclear (CTR) applications. *Nature* **239**.

Orszag, S. A. 1980 Spectral methods for problems in complex geometries. *J. Comput. Phys.* **37**, 70–92.

Pakula, R. & Sigel, R. 1985 Self-similar expansion of dense matter due to heat transfer by nonlinear conduction. *Phys. Fluids* **28** (1), 232–44.

Paolucci, S. 1982 On the filtering of sound from the Navier–Stokes. SAND82-8257. Sandia National Laboratories.

Peyret, R. 2002 *Spectral Methods for Incompressible Viscous Flow*. Springer.

Piriz, A. R., Sanz, J. & Ibañez, F. 1997 Rayleigh–Taylor instability of steady ablation fronts: the discontinuity model revisited. *Phys. Plasmas* **4** (4), 1117–1126.

Reinicke, P. & Meyer-ter-Vehn, J. 1991 The point explosion with heat conduction. *Phys. Fluids* A **3**, 1807–1818.

Renaud, F. & Gauthier, S. 1997 A dynamical pseudo-spectral domain decomposition technique: application to viscous compressible flows. *J. Comput. Phys.* **131**, 89–108.

Sanmartín, J. R. & Barrero, A. 1978*a* Self-similar motion of laser half-space plasmas. I. Deflagration regime. *Phys. Fluids* **21** (11), 1957–1966.

Sanmartín, J. R. & Barrero, A. 1978*b* Self-similar motion of laser half-space plasmas. II. Thermal wave and intermediate regimes. *Phys. Fluids* **21** (11), 1967–1971.

Sanz, J., Piriz, A. R. & Tomasel, F. G. 1992 Self-similar model for tamped ablation driven by thermal radiation. *Phys. Fluids* B **4** (3), 683–692.

Thompson, P. A. 1988 *Compressible-Fluid Dynamics*. Advanced Engineering.

Velikovich, A. L., Dahlburg, J. P., Gardner, J. H. & Taylor, R. J. 1998 Saturation of perturbation growth in ablatively driven planar laser targets. *Phys. Plasmas* **5** (5).

Velikovich, A. L., Dahlburg, J. P., Schmitt, A. J., Gardner, J. H., Phillips, L., Cochran, F. L., Chong, Y. K., Dimonte, G. & Metzler, N. 2000 Richtmyer–Meshkov-like instabilities and early-time perturbation growth in laser targets and Z-pinch loads. *Phys. Plasmas* **7** (2).

Zel'dovich, Y. & Raizer, Y. 1967 *Physics of Shock Waves and High-Temperature Hydrodynamic Phenomena*. Academic.